The Astrophysical Journal, 598:720–740, 2003 December 1

PROBING DARK ENERGY WITH BARYONIC ACOUSTIC OSCILLATIONS FROM FUTURE LARGE GALAXY REDSHIFT SURVEYS

Hee-Jong Seo and Daniel J. Eisenstein
Steward Observatory, University of Arizona, 933 North Cherry Avenue, Tucson, AZ 85721; hseo@as.arizona.adu, deisenstein@as.arizona.edu
Received 2003 May 26; accepted 2003 July 31

ABSTRACT

We show that the measurement of the baryonic acoustic oscillations in large high-redshift galaxy surveys offers a precision route to the measurement of dark energy. The cosmic microwave background provides the scale of the oscillations as a standard ruler that can be measured in the clustering of galaxies, thereby yielding the Hubble parameter and angular diameter distance as a function of redshift. This, in turn, enables one to probe dark energy. We use a Fisher matrix formalism to study the statistical errors for redshift surveys up to $z = 3$ and report errors on cosmography while marginalizing over a large number of cosmological parameters, including a time-dependent equation of state. With redshift surveys combined with cosmic microwave background satellite data, we achieve errors of 0.037 on Ω_X, 0.10 on $w(z = 0.8)$, and 0.28 on $dw(z)/dz$ for the cosmological constant model. Models with less negative $w(z)$ permit tighter constraints. We test and discuss the dependence of performance on redshift, survey conditions, and the fiducial model. We find results that are competitive with the performance of future Type Ia supernova surveys. We conclude that redshift surveys offer a promising independent route to the measurement of dark energy.

Subject headings: cosmological parameters — cosmology: theory — distance scale — large-scale structure of universe — methods: statistical

On-line material: color figures

1. INTRODUCTION

Recent observations of distant Type Ia supernovae (SNe Ia) have reached the startling conclusion that the expansion of the universe is accelerating (Perlmutter et al. 1999; Riess et al. 1998, 2001; Tonry et al. 2003). Under the premise of Friedmann equations, this implies the existence of an energy component, christened dark energy, with negative pressure (Ratra & Peebles 1988; Frieman et al. 1995). The detailed characterization of the accelerated expansion and its cause is now one of the main subjects of cosmology. Dark energy presently constitutes about $\frac{2}{3}$ of the total energy density of the universe, and its physical property is often parameterized by the ratio of pressure to density, that is, the equation of state (Steinhardt 1997; Turner & White 1997). A cosmological constant (for a review see Carroll, Press, & Turner 1992) has a constant equation of state of -1, while general quintessence models (Caldwell et al. 1998) and other theories (Zlatev, Wang, & Steinhardt 1999; Bucher & Spergel 1999; Armendariz-Picon, Mukhanov, & Steinhardt 2000; Boyle, Caldwell, & Kamionkowski 2002; Gu & Hwang 2001; Kasuya 2001; Bilic, Tupper, & Viollier 2002; Deffayet, Dvali, & Gabadadze 2002; Freese & Lewis 2002) typically allow equations of state with a redshift dependence. Measuring the time dependence of the equation of state, as well as its present density, is an essential step in identifying the physical origin of dark energy (Hui, Stebbins, & Burles 1999; Cooray & Huterer 1999; Huterer & Turner 1999, 2001; Newman & Davis 2000; Haiman, Mohr, & Holder 2001; Maor, Brustein, & Steinhardt 2001; Wang & Garnavich 2001; Kujat et al. 2002; Maor et al. 2002; Newman et al. 2002; Weller & Albrecht 2002; Frieman et al. 2003; Linder & Huterer 2003). Because of the inertness and the relative smoothness of this energy component, as commonly believed in the standard pictures of dark energy, the best cosmological probe of dark energy is the expansion history of the universe, measured by the Hubble parameter and angular diameter distance.

In this paper we demonstrate that the Hubble parameter $H(z)$ and angular diameter distance $D_A(z)$ can be measured to excellent precision by using the baryonic acoustic oscillations imprinted in the large-scale structure of galaxies. We are familiar with this signature as the now-famous Doppler peaks in the anisotropies of the cosmic microwave background (CMB; Peebles & Yu 1970; Bond & Efstathiou 1984; Miller et al. 1999; de Bernardis et al. 2000; Hanany et al. 2000; Halverson et al. 2002; Benoît et al. 2003; Bennett et al. 2003); however, the same structure is predicted to be present in the late-time clustering of galaxies as a series of weak modulations in the amplitude of fluctuations as a function of scale (Peebles & Yu 1970; Bond & Efstathiou 1984; Holtzman 1989; Hu & Sugiyama 1996). The physical scale of the oscillations is determined by the matter and baryon densities, which can be precisely measured with CMB anisotropy data. This calibrates the acoustic oscillations as a standard ruler (Eisenstein, Hu, & Tegmark 1998; Eisenstein 2003). The observed length scales of oscillations in the transverse and line-of-sight directions in a galaxy redshift survey then determine the angular diameter distance $D_A(z)$ and the Hubble parameter $H(z)$ as functions of redshift. As an oscillatory feature, the acoustic signature is less susceptible to general systematic errors and distortions; however, only large surveys map enough cosmic volume to achieve the precision required to detect these features. In addition, the features along the line-of-sight clustering are on sufficiently small scales that resolving them requires an accurate measurement of redshift, motivating the need for spectroscopic redshift surveys. Surveys at higher redshift are preferred so as to avoid the erasure of the oscillatory features by nonlinear structure formation (Jain & Bertschinger 1994; Meiksin, White, & Peacock 1999; Meiksin & White 1999). Recent analyses of large surveys may be beginning to

reveal these features (Percival et al. 2001; Miller, Nichol, & Batuski 2001).

There have been numerous studies on how the combination of CMB anisotropy data and large-scale structure data, either present (Scott, Silk, & White 1995; Gawiser & Silk 1998; Lange et al. 2001; Tegmark, Zaldarriaga, & Hamilton 2001; Efstathiou et al. 2002; Spergel et al. 2003) or future (Hu, Eisenstein, & Tegmark 1998; Eisenstein et al. 1998; Wang, Spergel, & Strauss 1999; Eisenstein, Hu, & Tegmark 1999; Popa, Burigana, & Mandolesi 2001), can constrain cosmological parameters. These studies have considered an increasing number of parameters and degeneracies and build on a body of work in CMB parameter estimation (Knox 1995; Jungman et al. 1996; Zaldarriaga, Spergel, & Seljak 1997; Bond, Efstathiou, & Tegmark 1997). However, most previous work on galaxy surveys has concentrated on low redshifts and used spherically averaged power spectra. The spherical assumption neglects the effects of redshift distortions and cosmological distortions. Including the nonisotropic information in the clustering of galaxies allows one to recover these effects (Ballinger, Peacock, & Heavens 1996; Heavens & Taylor 1997; Hatton & Cole 1999; Taylor & Watts 2001; Matsubara & Szalay 2002, 2003).

In this paper we design large galaxy redshift surveys at high redshift that can recover the acoustic peaks with a level of precision that allows us to put competitive constraints on the dark energy. We describe the constraints in terms of statistical errors using a Fisher matrix treatment of the full three-dimensional power spectra. We study galaxy surveys at $z = 0.3$, $z \sim 1$, and $z = 3$ so as to have access to cosmological distortions across a wide range of cosmic history. As our goal is to optimize survey design based on realistic statistical errors, we try to be conservative in our methodology. For example, we adopt ungenerous values for the nonlinear scales and marginalize over a large number of cosmological parameters. We present the predicted performance of our baseline surveys with constraints derived for $H(z)$ and $D_A(z)$ and then propagate these errors to the constraints on the dark energy parameters at our fiducial cosmology model, ΛCDM. This work extends that of Blake & Glazebrook (2003) in that we have used a full Fisher matrix formalism to treat the cosmological constraints from large-scale structure, CMB anisotropies, and SN data simultaneously and that we have considered time-variable equations of state. It differs from Linder (2003a) in that it is an explicit treatment of the survey data sets in addition to a discussion of dark energy parameter estimation. Contemporaneously with this paper, Hu & Haiman (2003) used a Fisher matrix technique similar to ours to study the performance of a mid-redshift cluster survey. The two analyses differ in numerous details.

In § 2 we discuss the details of the physics to probe dark energy. In § 3 we present the survey condition we assume and our Fisher information matrix methodology. We present and discuss our results in § 4. We consider variations in survey design and the fiducial model. We compare the performance to an SN survey and to pure imaging surveys.

2. FROM BARYONIC OSCILLATIONS TO DARK ENERGY

2.1. *Cosmography and Dark Energy*

The expansion history of the universe can be written as the redshift $z(t)$ as a function of time, which in turn is completely specified by the Hubble parameter $H(z)$ as a function of redshift. We will probe the expansion history by measuring $H(z)$ and the angular diameter distance $D_A(z)$.

The evolution of dark energy density can be described by the present-day dark energy density Ω_X and the equation of state of dark energy, $w_X(z)$ (Steinhardt 1997; Turner & White 1997), where

$$w_X(z) = \left.\frac{p_X}{\rho_X}\right|_z . \tag{1}$$

This yields an energy density as a function of redshift

$$\rho_X(z) = \rho_X(0) \exp\left[3\int_0^z \frac{1+w(z)}{1+z}dz\right] . \tag{2}$$

Assuming a flat universe, $D_A(z)$ and $H(z)$ are then related to the dark energy density through

$$H(z) = H_0\sqrt{\Omega_m(1+z)^3 + \Omega_X \exp\left[3\int_0^z \frac{1+w(z)}{1+z}dz\right]}$$
$$= \sqrt{\frac{\Omega_m H_0^2}{1-\Omega_X}}\sqrt{\Omega_m(1+z)^3 + \Omega_X \exp\left[3\int_0^z \frac{1+w(z)}{1+z}dz\right]} , \tag{3}$$

$$D_A(z) = \frac{c}{1+z}\int_0^z \frac{dz}{H(z)} , \tag{4}$$

where Ω_X is the present-day dark energy fraction with respect to the critical density and $H_0 = h \times 100$ km s^{-1} Mpc^{-1}, which is the present-day Hubble constant. In a general sense, $H(z)$ and $D_A(z)$ are the fundamental observables, to be interpreted here as Ω_X and $w(z)$. The comoving sizes of an object or a feature at redshift z in line-of-sight ($r_\parallel$) and transverse ($r_\perp$) directions are related to the observed sizes Δz and $\Delta\theta$ by $H(z)$ and $D_A(z)$:

$$r_\parallel = \frac{c\Delta z}{H(z)} , \tag{5}$$

$$r_\perp = (1+z)D_A(z)\Delta\theta . \tag{6}$$

When the true scales, $r_\parallel$ and $r_\perp$, are known, measurements of the observed dimensions, Δz and $\Delta\theta$, give estimates of $H(z)$ and $D_A(z)$. The object is then known as a "standard ruler." Equations (5) and (6) can be applied equally well in Fourier space (inverted, of course).

It is well known that even if we do not know the scale of a feature, we can still extract the product $H(z)D_A(z)$ (Alcock & Paczynski 1979). The acoustic oscillation method presented here is not an Alcock-Paczynski method because we do know the scale of the sound horizon.

The cosmological feature to be measured need not be an actual object. Instead, we can use a statistical property of structure in many realizations such as correlation length (Ballinger et al. 1996; Matsubara & Szalay 2003). On large scales, features in the power spectrum may be more prominent and hence easier to use.

The equation of state $w(z)$ can be written as a derivative of $H(z)$ versus redshift, which in turn is a derivative of the angular diameter distance versus redshift (eqs. [3] and [4]). If we seek to measure not only the mean value of $w(z)$ but also its slope in redshift, we are adding yet another derivative to the process. In short, to measure the time variation of the equation of state, we must be able to measure the second derivative of $H(z)$ or the third derivative of the distance-redshift relation. As each derivative magnifies the

measurement noise in its parent function, we require enormous precision to proceed. In the context of galaxy surveys, this will drive us to require large volumes.

2.2. *Baryonic Acoustic Oscillations in the Matter Power Spectrum*

Baryonic acoustic oscillations are a generic feature of the power spectrum of large-scale structure and an excellent candidate for the standard ruler test. Prior to recombination, the baryons in the universe are locked to photons of the cosmic microwave background, and the photon pressure interacting against the gravitational instability produces a series of sound waves in the plasma. After recombination, the baryons and photons separate, but the effects of the acoustic oscillations remain imprinted in their spatial structure of the baryons and eventually the dark matter (Peebles & Yu 1970; Holtzman 1989; Hu & Sugiyama 1996; Eisenstein & Hu 1998). The resulting power spectrum is shown in Figure 1.

The physical length scale of the acoustic oscillations depends on the sound horizon of the universe at the epoch of recombination. The sound horizon is the comoving distance a sound wave can travel before recombination and depends simply on the baryon and matter densities. The relative heights of the acoustic peaks in the CMB anisotropy power spectra measure these densities to excellent accuracy, thereby producing an accurate measurement of the sound horizon (Eisenstein et al. 1998; Eisenstein 2003).

While the matter power spectrum is simply a product of the spectrum of primordial fluctuations and the modification of those fluctuations in later epochs, notably the radiation domination era and recombination, our observations of this power spectrum are complicated by the biases of galaxy clustering, the distortions from peculiar velocities, and the errors induced from reconstructing distances with the wrong cosmology. The latter two effects break the intrinsic statistical isotropy of the clustering of matter and introduce variations that depend on the angle of the wavevector to the line of sight.

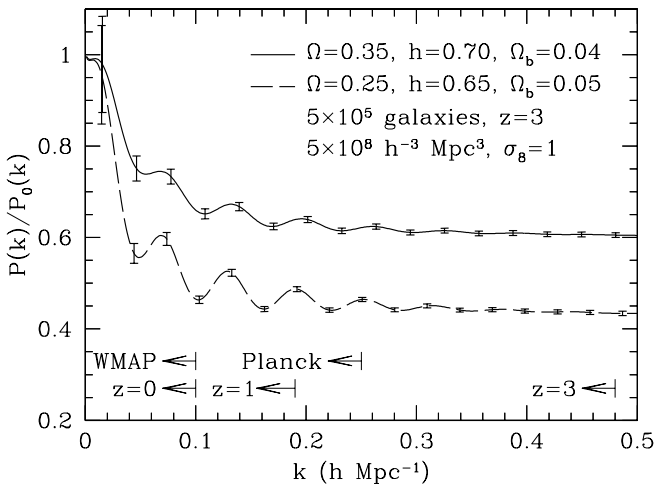

FIG. 1.—Linear power spectrum in two different cosmological models, $\Omega_m = 0.35$, $h = 0.70$, $\Omega_b = 0.04$ and $\Omega_m = 0.25$, $h = 0.65$, $\Omega_b = 0.05$. Each power spectrum has been divided by the zero-baryon power spectrum for that Ω_m and h. The series of acoustic oscillations is clearly seen. Lines at the bottom show the nonlinear scale, shortward of which the acoustic oscillations are washed out, as a function of redshift. The scales probed by the *WMAP* and *Planck* satellite measurements of primordial anisotropy are also shown. The error bars show the spherically averaged band power measurements from the $z = 3$ survey we present in § 3.1. [*See the electronic edition of the Journal for a color version of this figure.*]

In the absence of massive neutrinos (Bond & Szalay 1983), linear perturbation theory fixes the shape of the matter power spectrum in comoving coordinates and changes only the amplitude as the structure evolves. The growth function $G(z)$ rescales the amplitude of the fixed matter power spectrum to account for the growth of structure from the recombination to a redshift z. The growth function does depend on the details of dark energy. However, the subtle changes in the amplitude of the matter power spectrum are easily confused in galaxy redshift surveys with evolution in the bias of galaxies. While bias can be estimated from redshift distortions, recovering it to the 1% accuracy required for interesting constraints on dark energy is unlikely, especially in light of the systematic uncertainties of poorly known scale dependencies of the redshift distortion.

In principle, galaxy clustering bias could be arbitrary (Dekel & Lahav 1999); however, under the assumptions of local bias and Gaussian statistics for the density field, the bias on large scales should be independent of scale in the correlation function (Coles 1993; Scherrer & Weinberg 1998; Meiksin et al. 1999; Coles, Melott, & Munshi 1999). In the power spectrum, this appears as a constant multiplicative bias plus a constant additive offset (Seljak 2000). Moreover, even if the bias deviates from scale independence on linear or quasi-linear scales, it is very implausible for it to introduce oscillations in Fourier space on the acoustic scales, as this would correspond to a preferred length scale in real space of enormous size ($\gtrsim 30$ Mpc).

Redshift distortions are an angle-dependent distortion in power caused by the peculiar velocities of galaxies (Hamilton 1998 and references therein). On the largest scales, these distortions follow a simple form (Kaiser 1987) in which the distortion is an angle-dependent, multiplicative change in power. We follow this prescription. In reality, redshift distortions are nonlinear, including the finger-of-God effects on small scales. However, these deviations have no large preferred length scale and will not disturb analysis of the acoustic oscillations.

Whereas the linear theory redshift distortions are an angle-dependent modulation in the power spectrum amplitude, the cosmological distortion resulting from an incorrect mapping of observed separations to true separations produces a distortion in scale. Spherical features in power become ellipsoids under the false cosmology. Were the power spectrum a simple power law, the cosmological and redshift distortions would be indistinguishable in their quadrupole signatures and difficult to separate overall. Fortunately, the matter power spectrum is not a simple power law and the slow rollover in the power lifts some of the degeneracy between the two distortions (Ballinger et al. 1996; Matsubara & Szalay 2003). However, strong features such as baryonic acoustic oscillations are far more powerful at separating the two because, with a rapidly varying function, the difference between dilating the scale and modulating the amplitude is very stark.

Unfortunately, the use of baryonic oscillations as a standard ruler to derive $D_A(z)$ and $H(z)$ is not always straightforward. The nonlinear gravitational growth of perturbation in the large-scale structure erases the primordial features on smaller scales (large wavenumbers). This occurs when perturbations on a given scale become of order unity in

amplitude, leading to nonlinear coupling between Fourier modes. The obscuration by nonlinearity moves to a larger scale as the universe evolves, and today the scale corresponds to wavelengths of about 60 h^{-1} Mpc, enough to wipe out all but the first and a part of the second of the acoustic oscillations (Meiksin et al. 1999). At higher redshift, the process is less advanced, and we can recover the primordial signals on smaller scales, including the full series of acoustic oscillations. For example, at $z = 3$, we should be able to recover primordial information to roughly 12 h^{-1} Mpc (a factor of 2 smaller than what can be found in the primary anisotropies of the microwave background), which means that many acoustic oscillations can be preserved outside of the nonlinearity region. In practice, we will be limited to about four peaks because Silk damping makes the higher harmonics smaller than our expected power spectrum measurements. Figure 1 shows the nonlinear scale as a function of redshift, as well as the scales probed by the CMB primary anisotropies as measured by the *WMAP* and *Planck* satellites. While low-redshift surveys such as the Sloan Digital Sky Survey (SDSS; York et al. 2000) are much more restricted by the nonlinearity of clustering, they do provide a valuable data point at an epoch where the dark energy is largest.

It is worth comparing the measurements from future redshift surveys to those inferred from the observations of SNe Ia (Riess et al. 1998, 2001; Perlmutter et al. 1999; Tonry et al. 2003). The SN surveys measure the luminosity distance as a function of redshift, which in standard cosmologies is equivalent to the angular diameter distance. While this requires an additional derivative to extract $w(z)$ relative to measures of $H(z)$, future SN programs such as the *SNAP* satellite could achieve extremely good precision on distances at redshifts below 1.7. While the cosmological implications of low-redshift acoustic oscillations and SN distances are partially degenerate, the systematic errors will be completely different.

In summary, the baryon acoustic oscillations form a standard ruler that can be measured through galaxy redshift surveys to yield $H(z)$ and $D_A(z)$ at a range of redshifts. The scale of the acoustic oscillations is expected to be very robust to nonlinear gravitational clustering, galaxy biasing, and redshift distortions, making this a potentially clean probe of cosmography. If we can show that the distance measurements can be made to sufficient precision, then acoustic oscillations will offer a new and independent path to the quantification of dark energy.

3. METHODOLOGY

In this section we present the methodology of constraining the dark energy through distance measurements derived from surveys of galaxy clustering. To probe the time evolution of the dark energy, we need galaxy power spectra at a variety of redshifts. We design surveys at six different redshift bins, ranging from 0.3 to 3. We then present our methodology for computing the statistical errors from these surveys and from our ancillary data sets. We do this using a Fisher matrix formalism in a parameterized cosmological model.

3.1. *Statistical Error on the Power Spectrum*

To estimate errors on $D_A(z)$ and $H(z)$, we begin with the errors on the power spectrum that result from a galaxy survey. Under Gaussian approximations, the statistical errors are a combination of the limitations of the finite volume of the survey and the incomplete sampling of the underlying density field. These are known as sample variance and shot noise, respectively. At a single wavevector $\boldsymbol{k}$, the intrinsic statistical error associated with power is the sum of the power and shot noise (Feldman, Kaiser, & Peacock 1994; Tegmark 1997)

$$\frac{\sigma_P}{P} = \frac{P + 1/n}{P} \ . \tag{7}$$

Here $1/n$ is a white shot noise from the Poisson sampling of the density field assuming that the comoving number density n is constant in position. If the shot-noise term exceeds the true power, that is, when nP is less than unity, then shot noise will significantly compromise the measurement. Note that nP depends on wavenumber.

However, when the survey volume is finite, the power at nearby wavevectors is highly correlated, and one can think of discretizing the Fourier modes of the density field into cells in Fourier space whose volume is $(2\pi)^3/V_{\rm survey}$, where $V_{\rm survey}$ is the comoving survey volume. Neglecting boundary effects, the statistical power of the survey is well approximated by treating these cells as independent (Tegmark 1997). If the survey volume is large enough that the discretization scale is small compared to the regions of wavevector space over which the power spectrum is constant, then we can estimate the band power as averaged over a finite volume in Fourier space. We parameterize this by the wavenumber range Δk and the range $\Delta\mu$ of the cosine of the angle between the wavevector and the line of sight. The volume in Fourier space is simply $2\pi k^2 \Delta k \Delta\mu$ and the number of modes is $2\pi k^2 \Delta k \Delta\mu V_{\rm survey}/(2\pi)^3$. However, because the density field is real valued, the Fourier modes $\boldsymbol{k}$ and $-\boldsymbol{k}$ are not independent, which reduces the number of independent modes by a factor of 2. The fractional error on the band power is then (Feldman et al. 1994; Tegmark 1997)

$$\frac{\sigma_P}{P} = 2\pi \sqrt{\frac{2}{V_{\rm survey} k^2 \Delta k \Delta\mu}} \left(\frac{1 + nP}{nP}\right) \ , \tag{8}$$

where P is the average comoving band power. This fractional error on power spectrum (eq. [8]) enters in the Fisher matrix and will be propagated to the errors on parameters that we want to calculate.

3.2. *The Fisher Information Matrix for Galaxy Redshift Surveys*

Given the uncertainties of our observations, we now want to propagate these errors to compute the precision of constraints on cosmological parameters. The Fisher information matrix provides a useful method for doing this (for a review see Tegmark, Taylor, & Heavens 1997). The method takes as input a set of observables and a parameterized theoretical model to predict those observables. We denote the parameters as $p_1, \ldots, p_N$. The Fisher information matrix incorporates the likelihood function of the observables to yield the minimum possible errors on an unbiased estimator of a given parameter, given that the true values of the parameters are those of a so-called fiducial model. Mathematically, these minimum errors are simply the square roots of the diagonal elements of the inverse of the Fisher matrix.

Assuming the likelihood function for the band powers of a galaxy redshift survey to be Gaussian, the Fisher matrix can be approximated as (Tegmark 1997)

$$F_{ij} = \int_{\boldsymbol{k}_{\rm min}}^{\boldsymbol{k}_{\rm max}} \frac{\partial \ln P(\boldsymbol{k})}{\partial p_i} \frac{\partial \ln P(\boldsymbol{k})}{\partial p_j} V_{\rm eff}(\boldsymbol{k}) \frac{d\boldsymbol{k}}{2(2\pi)^3} = \int_{-1}^{1} \int_{\boldsymbol{k}_{\rm min}}^{\boldsymbol{k}_{\rm max}} \frac{\partial \ln P(k,\mu)}{\partial p_i} \frac{\partial \ln P(k,\mu)}{\partial p_j} V_{\rm eff}(k,\mu) \frac{2\pi k^2\, dk\, d\mu}{2(2\pi)^3}\,, \tag{9}$$

where the derivatives are evaluated at the parameter values of the fiducial model and $V_{\rm eff}$ is the effective volume of the survey, given as

$$V_{\rm eff}(k,\mu) = \int \left[\frac{n(\boldsymbol{r})P(k,\mu)}{n(\boldsymbol{r})P(k,\mu)+1}\right]^2 d\boldsymbol{r} = \left[\frac{nP(k,\mu)}{nP(k,\mu)+1}\right]^2 V_{\rm survey}\,, \tag{10}$$

where the last equality holds only if the comoving number density n is constant in position. Here $\mu = \boldsymbol{k}\cdot\hat{\boldsymbol{r}}/k$, where $\hat{\boldsymbol{r}}$ is the unit vector along the line of sight and $\boldsymbol{k}$ is the wavevector with norm $k = |\boldsymbol{k}|$. As a result of azimuthal symmetry around the line of sight, the power spectrum $P(\boldsymbol{k})$ depends only on k and μ, but of course it has an implicit dependence on the cosmological parameters p_i. Equations (9) and (10) are not fully general, as we have assumed a flat-sky approximation in which the survey box is imagined to be far from the observer. Given that the clustering scales of interest will subtend small angles on the sky in all of our designed surveys, this is an appropriate approximation.

We have not included information from all wavenumbers in our equation (9). Wavenumbers smaller than $k_{\rm min}$ or larger than $k_{\rm max}$ have been dropped. We use $k_{\rm max}$ to exclude information from the nonlinear regime, where our linear power spectra are inaccurate. We adopt conservative values for $k_{\rm max}$ by requiring $\sigma(R) = 0.5$ at a corresponding $R = \pi/2k$. At $z = 0$, this sets $k_{\rm max} = 0.1\ h\ {\rm Mpc}^{-1}$, which is consistent with the numerical simulations of Meiksin et al. (1999) and noticeably smaller than that used by most published analyses of past redshift surveys. The $k_{\rm max}$ values used for different redshift bins are listed in Table 1. The maximum scale of the survey $k_{\rm min}$ has almost no effect on the results; we adopt $k_{\rm min} = 0$.

In principle, the mapping from the observed galaxy separations to the physical separations and wavevectors depends on the cosmological functions $D_A(z)$ and $H(z)$, which are varying continuously across the redshift range of the survey. When doing an analysis of real data, one would of course include this variation. For our forecasts, however, we opt to break the survey into a series of slabs in redshift, inside of which we treat the survey region as a fixed Euclidean geometry, with a constant D_A and H and a rectilinear division between the transverse and radial directions. This approximation is harmless as regards the statistical power of the survey or the parameter degeneracies involved. We use redshift bins that are narrow enough to finely sample the dark energy behavior.

3.3. *Parameters*

A Fisher matrix formalism relies on a detailed parameterization of its space of models. The performance forecasts are only as realistic as the generality of the permitted models. For our forecasts, we proceed in two stages. First, we define a very general parameterization based on CDM cosmologies and assigning independent parameters to each redshift bin. This permits us to forecast cosmographical constraints independent of any dark energy model. Second, we introduce a smaller set of parameters to describe dark energy by relating the distances in different redshift bins. This will allow us to combine many distance measurements into constraints on a low-dimensional dark energy model.

3.3.1. *Cold Dark Matter Cosmography*

We use a very general space of CDM models. Our parameters include the matter density ($\Omega_m h^2$), baryon density ($\Omega_b h^2$), matter fraction (Ω_m), the optical depth to reionization (τ), the spectral tilt (n_s), the tensor-to-scalar ratio (T/S), and the normalization ($\ln A_S^2$). Our fiducial model is $\Omega_m = 0.35$, $h = 0.65$, $\Omega_\Lambda = 0.65$, $\Omega_K = 0$, $\Omega_b h^2 = 0.021$, $\tau = 0.05$, $n_s = 1$, and $T/S = 0$.

We supplement this model with many additional parameters to describe the behavior at each redshift. For the CMB, we include an unknown angular distance $D_{A,{\rm CMB}}$ to the last scattering surface at $z = 1000$. For each redshift survey bin, we add a parameter for the angular diameter distance ($\ln D_A$), the Hubble parameter ($\ln H$), the linear growth function ($\ln G$), the linear redshift distortion ($\ln \beta$), and an unknown shot noise $P_{\rm shot}$. With five additional parameters in each of six redshift bins, the total number of parameters for the CMB and galaxy surveys is 38. The fiducial values of these parameters are evaluated at the central redshift of each slice, and the fiducial values of β are computed from the

TABLE 1
Baseline Survey Parameters

Survey	z	$k_{\rm max}$ (h Mpc^{-1})	$V_{\rm survey}$[a] (h^{-3} Gpc^3)	$N_{\rm gal}$[b] (10^5)	Bias[c]	$P(0.2\,h\,{\rm Mpc}^{-1})$ (h^{-3} Mpc^3)	$P(k_{\rm max})$ (h^{-3} Mpc^3)	nP ($0.2\,h$ Mpc^{-1})	nP ($k_{\rm max}$)
SDSS	0.3	0.11	1.0	1.0	2.13	...	22900	...	2.29
$z \sim 1$	0.6	0.15	0.29	1.44	1.25	...	4660	...	2.33
	0.8	0.17	0.40	2.00	1.40	...	3590	...	1.80
	1.0	0.19	0.49	2.46	1.55	...	3090	...	1.55
	1.2	0.21	0.56	2.82	1.70	2860	2620	1.43	1.31
$z = 3$	3.0	0.53	0.50	5.0	3.30	2950	430	2.95	0.43

[a] 1000 deg^2 for $z \sim 1$; 140 deg^2 for $z = 3$.
[b] The number density n: $10^{-4}\ h^3$ Mpc^{-3} for SDSS, $5 \times 10^{-4}\ h^3$ Mpc^{-3} for $z \sim 1$, and $10^{-3}\ h^3$ Mpc^{-3} for $z = 3$.
[c] Calculated using eq. (17) assuming $\sigma_{8,{\rm mass}} = 0.9$ at $z = 0$, $\sigma_{8,g} = 1.8$ for SDSS, $\sigma_{8,g} = 1$ for $z \sim 1$ and $z = 3$.

values of the bias as found from the fiducial values of the observed galaxy clustering.

By keeping $D_A(z)$, $H(z)$, and $G(z)$ as separate parameters at each redshift, we have avoided any assumption thus far of a specific dark energy model. The only cross talk between the various distances and amplitudes occurs through the parameters of $\Omega_m h^2$, $\Omega_b h^2$, and n_s that set the shape of the galaxy power spectrum. In other words, a good constraint at one redshift implies nothing for another redshift because we have specified nothing about the behavior of the distances as a function of redshift.

The unknown white shot noise $P_{\rm shot}$ is a shot noise in the observed power spectrum at each redshift bin that remains even after the conventional shot noise of inverse number density is subtracted from the observed power spectrum. These terms can arise from galaxy clustering bias (Seljak 2000) even on large scales because of the zero-lag terms in the correlation function, which are permitted in the theories of local bias (Coles 1993).

The partial degeneracy between redshift distortions and cosmological distortions requires care because the broadband aspects of the observed power spectra are extremely well constrained in these surveys. If one knew the precise amplitude of the matter power spectrum at a given redshift, then one would know the bias to high precision. This would yield the value of β, and knowing this, we could extract the cosmological distortions from the quadrupole distortions of the observed power. Unfortunately, we do not regard this as a robust cosmological test. Nonlinear redshift distortions are not well understood, particularly in the context of poorly constrained bias models. We seek to isolate our measurement of the cosmological distortions from overly optimistic assumptions about redshift distortions. The unknown growth functions and shot noises aid in this separation; the latter contributes because a white noise limits the localization of a power-law break in a smooth power spectrum. We do not use the recovered growth functions in our dark energy fits. We return to this topic in § 4.4.

3.3.2. *From Cosmography to Dark Energy*

We next wish to define a more restricted parameterization for the study of dark energy. We do this through a simple parameterization for the equation of state $w(z)$. The equation of state of a cosmological constant has $w = -1$ at all times, whereas quintessence models have $w > -1$, generically with time dependence. While the most important distinction of dark energy models would be to decide whether $w = -1$ or not, we also want to develop methods for tracking the time dependence. As a simplest approach, we assumed a linear equation of state in redshift (eq. [11]):

$$w(z) = w_0 + w_1 z \ . \tag{11}$$

Our choice of parameters for a dark energy is Ω_X (eq. [3]), w_0, and w_1. Other choices for parameterizing the free function $w(z)$ have been explored in Tegmark (2001), Linder (2003b), and Huterer & Starkman (2003).

We used a variety of dark energy fiducial models in this paper. The parameters of these models are listed in Table 2. We will focus most of our attention on a ΛCDM model with $\Omega_X = 0.65$, $w_0 = -1$, and $w_1 = 0$ and on a comparison model (model 2) with $w_0 = -\frac{2}{3}$. The primary difference between these is that dark energy remains more important at higher redshift in the $w = -\frac{2}{3}$ model. We consider four models with redshift-dependent equations of state. All have $w_1 > 0$, so that dark energy emerges at higher redshift than we would infer from w today. In detail, we truncate the increase in w at early times by setting $dw/dz = 0$ at $z > 2$ so that the value of w at $z > 2$ is simply $w(2)$. This is of minor importance because the dark energy is subdominant at these high redshifts, but it is necessary to avoid dark energy domination at early times. Models 5 and 6 have $w < -1$ today, which is a challenge to theory (but see Caldwell et al. 1998); we include these simply to study the phenomenological differences.

TABLE 2
DARK ENERGY MODELS

Model	w_0	w_1
1 (ΛCDM)	−1	0[a]
2	−2/3	0[a]
3	−2/3	1/6[b]
4	−1	1/3[b]
5	−4/3	1/3[b]
6	−1.15	1/3[b]

[a] The w_1 perturbations in these models were considered to extend to $z = \infty$; however, the derivatives were computed with infinitesimal step sizes, so the $w > 0$ region at high redshift was not an issue.

[b] The equation of state is $w(z) = w_0 + w_1 z$ for $z < z_t$ and $w_0 + w_1 z_t$ beyond. We use $z_t = 2$.

Equation (11) defines the equation of state today as the parameter w_0. Since the observations are all at higher redshift, the errors on w_0 are misleadingly poor because uncertainties in w_1 allow the value today to vary around a well-measured value at higher redshift. Errors on w at higher redshifts decrease to a minimum at a redshift $z_{\rm pivot}$, similar to the central redshift of the observations, and then increase again. For any choice of $z_{\rm pivot}$, we can recast the parameterization in equation (11) as

$$w(z) = w_0 + w_1 z = w\left(z_{\rm pivot}\right) + w_1\left(z - z_{\rm pivot}\right) \ . \tag{12}$$

At this redshift of minimum error, the covariance between $w(z_{\rm pivot})$ and w_1 vanishes, so that the two parameters are statistically independent. The value of $z_{\rm pivot}$ can be computed from the covariance matrix of w_0 and w_1 via the method in Appendix A of Eisenstein et al. (1999).

3.4. *Completion and Transformation of Fisher Matrices*

We must complete our formula (eq. [9]) for the Fisher information matrix for galaxy surveys by identifying the power spectrum for the corresponding redshift bin. $P(\boldsymbol{k})$ in equation (9) is a three-dimensional galaxy redshift power spectrum, to be reduced to two dimensions by symmetry. When we reconstruct our measurements of galaxy redshifts and positions using a particular reference cosmology, which differs from the true cosmology, the observed power spectrum is

$$P_{\rm obs}\left(k_{{\rm ref}\perp}, k_{{\rm ref}\parallel}\right) = \frac{D_A(z)_{\rm ref}^2 H(z)}{D_A(z)^2 H(z)_{\rm ref}} P_{\rm true}\left(k_\perp, k_\parallel\right) + P_{\rm shot} \ . \tag{13}$$

Here values of D_A and H in the reference cosmology are distinguished by the subscript "ref," while those in the true cosmology have no subscript. The vector components $k_\perp$

and $k_\parallel$ are, respectively, the wavenumbers across and along the line of sight in the true cosmology. These are related to the wavenumbers calculated assuming the reference cosmology, by $k_{\mathrm{ref}\perp} = k_\perp D_A(z)/D_A(z)_{\mathrm{ref}}$ and $k_{\mathrm{ref}\parallel} = k_\parallel H(z)_{\mathrm{ref}}/H(z)$. The prefactor of distance ratios accounts for the difference in volume between the two cosmologies. We adopt the reference cosmology to be equal to our fiducial cosmology for simplicity.

Next, the true cosmology must be constructed, including the redshift distortions. We do this by scaling to $z = 0$:

$$P_{\mathrm{obs}}\left(k_{\mathrm{ref}\perp}, k_{\mathrm{ref}\parallel}\right) = \frac{D_A(z)_{\mathrm{ref}}^2 H(z)}{D_A(z)^2 H(z)_{\mathrm{ref}}} b^2 \left(1 + \beta \frac{k_\parallel^2}{k_\perp^2 + k_\parallel^2}\right)^2 \times \left[\frac{G(z)}{G(z=0)}\right]^2 P_{\mathrm{matter},z=0}(k) + P_{\mathrm{shot}}\,, \quad (14)$$

where the bias b is $\Omega_m(z)^{0.6}/\beta(z)$. The normalization used to derive the power spectrum at z is

$$P(k_{\mathrm{norm}}, z = 1000) = A_S^2 \frac{k_{\mathrm{norm}}}{k_{\mathrm{fid}}} \left[\frac{c}{H(1000)}\right]^4, \quad (15)$$

where $k_{\mathrm{fid}} = 0.025\ \mathrm{Mpc}^{-1}$ and $k_{\mathrm{norm}}^{-1} = 3000$ Mpc. The actual power spectrum and derivatives with respect to various parameters are reconstructed from equation (14), using the numerical methods and results at $z = 0$ from Eisenstein et al. (1999).

For the Fisher matrix of CMB, we assume errors for the *Planck* satellite including polarization from Eisenstein et al. (1999). With *Planck*, the fractional errors on $\Omega_m h^2$ and $\Omega_b h^2$ are 0.9% and 0.6%, respectively. Together, these more than suffice to calibrate the sound horizon to 1%. The recovered error on the angular diameter distance to $z = 1000$ is 0.2%.

For the Fisher matrix of SNe, we introduce 16 redshift bins, at 0.05 and at 0.3–1.7 by steps of 0.1, to represent the SN distance information. We assign 1% independent errors to each redshift point (i.e., 0.022 mag error in distance modulus), with an overall 5% uncertainty in the distance scale (since the SN method by itself gives only a relative distance measurement). The appropriate covariance matrix is constructed and then inverted to give the Fisher matrix. In practice, the uncertainty in the distance scale is substantially reduced from the 5% starting value by combination with the CMB because the CMB's measurement of $\Omega_m h^2$ is combined with the SN measurement of Ω_m to yield the Hubble constant itself.

Our SN model was chosen to give similar performance to that of the proposed *SNAP* mission (Aldering et al. 2002) but differs in fine detail from that of the *SNAP* team. One should note that our 16 redshift points are statistically independent, so that with modest rebinning we are asserting better than 0.01 mag calibration between low- and high-redshift SNe. This is well beyond the current state of the art and is essentially the design goal of the *SNAP* mission.

Once the Fisher matrices for all the constituent data sets are set, we must derive marginalized errors on $D_A(z)$ and $H(z)$ and eventually on the dark energy parameters. Figure 2 shows the steps of the procedure graphically. To begin, the Fisher matrices are summed up and inverted. The square roots of the diagonal terms of this inverse Fisher matrix are the marginalized errors on parameters. We marginalize over

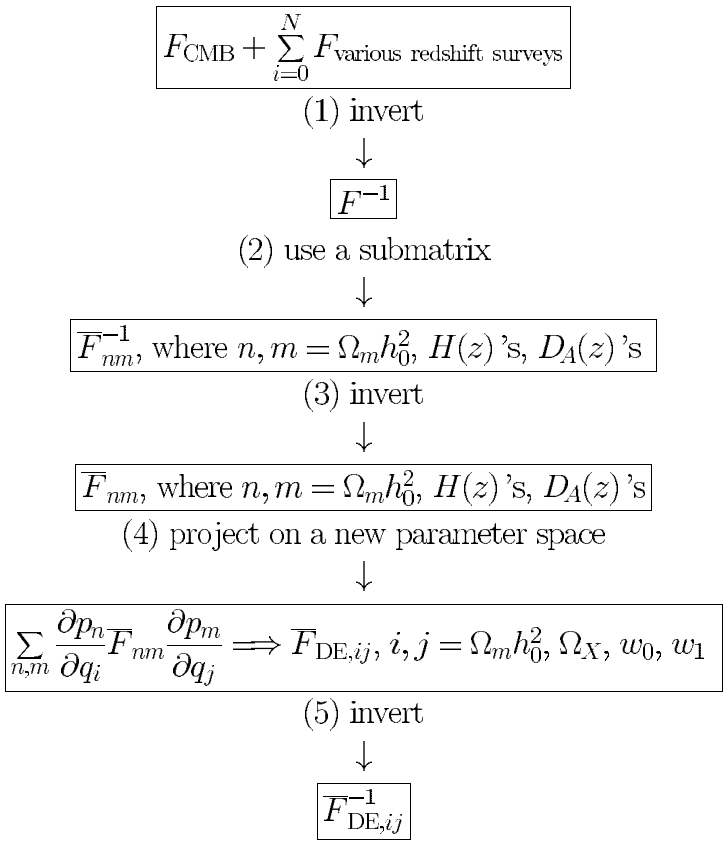

FIG. 2.—Flowchart of transformations of the Fisher matrices necessary to produce forecasts for the distance and dark energy parameters

and remove all the parameters that are not concerned with cosmography by taking a submatrix of the inverse Fisher matrix that includes only the rows and columns for $\Omega_m h^2$, $D_{A,\mathrm{CMB}}$, and the values of $H(z)$ and $D_A(z)$ at all redshift bins. This yields the covariance matrix for the cosmographical parameters. Although this is an intermediate result, it is very useful because it is independent of any dark matter model.

Next we project these errors through to the dark energy parameter space. Because the dark energy model makes explicit predictions for the various distances, we are *not* marginalizing over parameters. Rather, we are contracting the inverse of the covariance matrix, as one would do in a multidimensional χ^2 analysis. Hence, we invert the cosmographic covariance matrix to get a Fisher matrix $\bar{F}$ and contract this with the set of derivatives between the distances and the dark energy parameters ($\Omega_m h^2$, Ω_X, w_0, and w_1):

$$\bar{F}_{\mathrm{DE},ij} = \sum_{m,n} \frac{\partial p_n}{\partial q_i} \bar{F}_{nm} \frac{\partial p_m}{\partial q_j} \ , \tag{16}$$

where p_m are the distance parameters and q_i are the dark energy parameters. By inverting this Fisher matrix, we attain marginalized errors of dark energy parameters.

Equation (16) implies that the constraints on dark energy will be a combination of how well $D_A(z)$ and $H(z)$ are estimated within a given set of surveys and how effectively measurements of $D_A(z)$ and $H(z)$ can constrain dark energy. Figure 3 shows the derivatives of $D_A(z)$ and $H(z)$ with respect to the dark energy parameters. The left-hand panel is for ΛCDM; the right-hand panel is for model 2 ($w = -\frac{2}{3}$). One should remember that these are partial derivatives, so that three of the parameters $\Omega_m h^2$, Ω_X, w_0, and w_1 are being held fixed. The derivatives with respect to w_0 at fixed $\Omega_m h^2$, Ω_X, and w_1 have larger amplitude than those to w_1, meaning that D_A and H place better constraints on w_0 than on w_1. Based on the positions of maximum amplitudes, we expect that the information on w_1 comes from higher redshift than w_0. It is interesting to note that while an advantage of this acoustic oscillation method is to measure $H(z)$, the peaks of derivatives of $H(z)$ are at lower redshift where, as we will find, this method has poorer error bars. This tends to favor lower redshift probes such as SNe. It also implies that improving error bars on w_1 could be done by changing the redshift survey conditions at higher redshifts; that is, we may want to decrease error bars on $H(z)$ over the range $z = 1$–3 or on $D_A(z)$ at $z \gtrsim 2$. Comparing $w = -\frac{2}{3}$ to ΛCDM, one finds that the derivatives of both $D_A(z)$ and $H(z)$ peak at higher redshift when w is more positive. This will favor the galaxy surveys at higher redshift. Models 3–6 share this trend.

3.5. *Survey Design*

We want to design redshift surveys that are optimized to derive $D_A(z)$ and $H(z)$ within accessible resources. Our requirement is that we should be able to measure multiple acoustic peaks at various redshifts with high precision. In this section we define two sets of baseline surveys, with parameters in Table 1; we also consider variations on these in § 4.

To constrain the scale of the acoustic peaks, we clearly need superb precision in the power spectrum measurements. Equation (8) shows that the errors σ_P depend on the survey volume V_{survey} and on the number density n of objects in the survey. Of course, V_{survey} and n are limited by the available observational resources. If we assume that the observational resources scale with the total number of objects N, then at fixed N, σ_P/P has a minimum at $n = 1/P$ (Kaiser 1986) at each wavenumber k. However, near this minimum, the performance σ_P/P varies slowly, and a small deviation from the minimum incurs little penalty. For example, using $nP = 3$ or $nP = \frac{1}{3}$ increases the error by

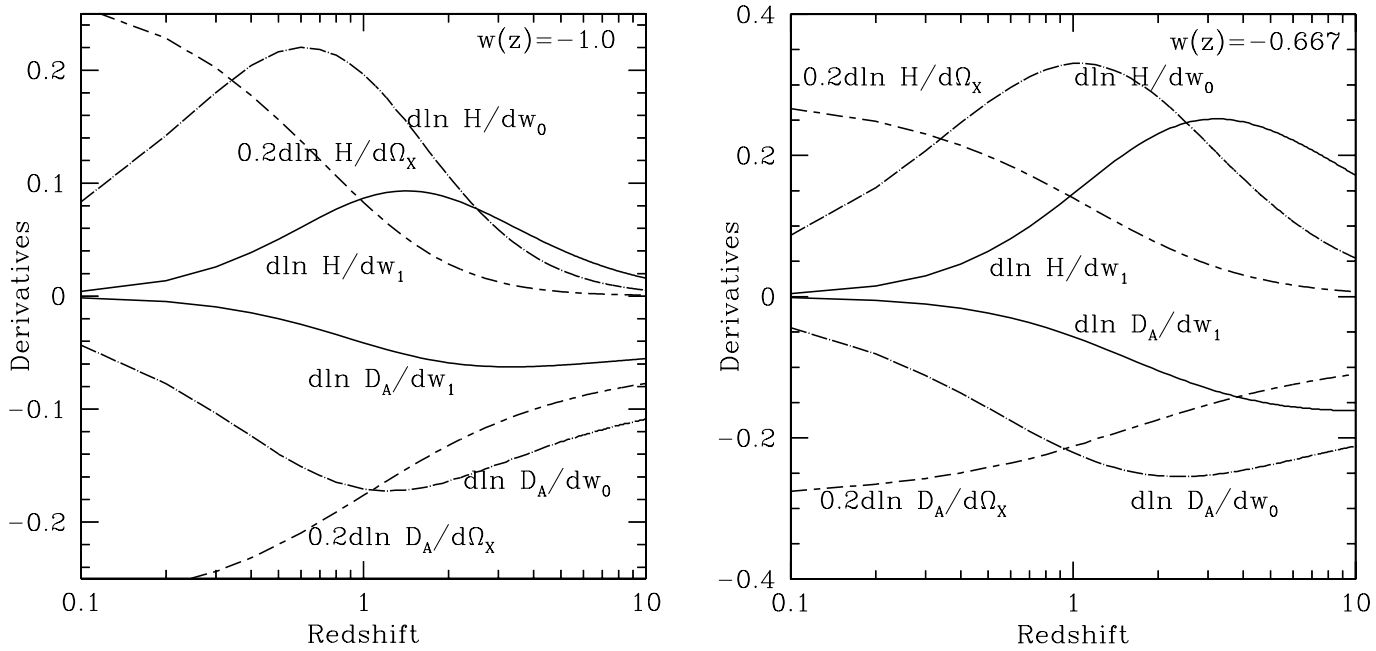

FIG. 3.—Derivatives of angular diameter distance (D_A) and Hubble parameter (H) with respect to Ω_X, w_0, and w_1 with $\Omega_m h^2$ being held fixed. As these are partial derivatives, one should remember that two of the three parameters are held fixed as well in each case. Notably, these are not the basis that leaves the CMB anisotropies unchanged. The Ω_X parameter is equivalent to Ω_m. *Left*: $w = -1.0$ (ΛCDM). *Right*: $w = -0.667$ (model 2).

only about 15%. With the relatively small dependence of error on nP near the minimum, we suggest that nP slightly larger than 1 is preferable for several reasons. First, larger nP increases the signal-to-noise ratio per pixel in the map. This enables computations beyond the power spectrum, e.g., for higher order correlations and non-Gaussianity. Second, it avoids some complication from the non-Gaussianity of the shot noise itself. Finally, it permits us to divide the survey into a few subsamples based on galaxy properties or other criteria with less loss in signal-to-noise ratio. This allows certain kinds of tests for systematic errors in the survey and for additional science return from the study of type-dependent galaxy bias.

On the other hand, it is possible that observation resources do not simply scale with the number of objects. For example, the field of view, i.e., $V_{\rm survey}$, may be more expensive than the number of spectroscopic targets. For a fixed survey volume, the error bars improve monotonically as targets are added, but the benefit saturates at $nP \gg 1$. For example, the error σ_P/P with $nP = 5$ is 1.7 times better than that of $nP = 1$ (at fixed volume), but only 20% worse than that of $nP = \infty$. In reality, increased target density is not free; higher number densities of objects require fainter objects (i.e., a deeper survey) and hence longer exposure times. Fortunately, the range of the number density we want is near the luminous tale of the luminosity functions, where the source counts are quite steep, and so it is rather easy to increase n moderately above $1/P$.

We conclude that $nP \sim 3$ is a good choice based on these considerations.

An additional question is which wavenumber k to use in calculating the value of nP. We are primarily interested in higher acoustic peaks, which occur around $k = 0.2\ h$ Mpc^{-1}. The power at this wavenumber is $\sim 2500\sigma_{8,g}^2\ h^{-3}$ Mpc^3, where $\sigma_{8,g}^2$ is the rms overdensity of the galaxies in spheres of 8 h^{-1} Mpc comoving radius. This gives $n = 4 \times 10^{-4}\sigma_{8,g}^{-2}\ h^3$ Mpc^{-3} for $nP = 1$. This is considerably less than the density of L^* galaxies. Power is higher at smaller k, so smaller densities would be optimal when measuring larger scales.

At $z \sim 3$, the obvious choice of galaxy targets are the Lyman break galaxies (Steidel et al. 1996). The value of $\sigma_{8,g}$ for these galaxies is measured to be about 1 (Steidel et al. 1998; Adelberger et al. 1998). The corresponding bias is calculated using

$$\sigma_{8,g} = b\sigma_{8,\rm mass}\sqrt{1 + \frac{2\beta}{3} + \frac{\beta^2}{5}}\,, \qquad (17)$$

assuming $\sigma_{8,\rm mass}$ of 0.9 for the matter distribution today and a linear redshift distortion effect (Kaiser 1987). For the number density, $10^{-3}\ h^3$ Mpc^{-3} is used so that $nP \approx 3$ at $k = 0.2\ h$ Mpc^{-1}. As an aside, a density $nP(0.2\ h$ Mpc$^{-1}) > 1$ is particularly valuable at $z = 3$ because the nonlinear scale has receded to much smaller scales ($k_{\rm max} \approx 0.5\ h$ Mpc^{-1}!). To make full use of the survey at all linear scales, we need a larger n. For our baseline survey, we adopt a total comoving volume of $0.5\ h^{-3}$ Gpc^3, which gives enough resolution and the precision to recover the first four acoustic peaks (Fig. 1). At this redshift, the comoving volume between $z = 2.5$ and 3.5 is 960 h^{-3} Mpc^3 arcmin^{-2}, yielding a total survey field of 140 deg^2. The areal number density is 1 galaxy arcmin^{-2}, similar to the depth of Steidel et al. (1998).

At $z \sim 1$, the choice of galaxy target is less obvious. One could reasonably use either giant elliptical galaxies or luminous star-forming galaxies. Luminous early-type galaxies have the advantage of high bias, probably $\sigma_{8,g} > 1$, and strong 4000 Å breaks, but getting the redshift does require detecting this continuum break, which requires longer integration times. Later type galaxies may be less biased, meaning that we need a larger number density, but they have strong 3727 Å emission lines, which can often be identified because the line is a doublet. For either case, we assume $\sigma_{8,g} = 1$ and $n = 5 \times 10^{-4}\ h^3$ Mpc^{-3}. This makes nP at $k \sim 0.2\ h$ Mpc^{-1} slightly bigger than 1, which means that nP will be at our desired value for the meaty part of the linear regime. From $z = 0.5$ to 1.3, there is a comoving volume of $480\ h^{-3}$ Mpc^3 arcmin^{-2}, leading to a surface density of 0.24 galaxies arcmin^{-2}. We assumed a total survey field of 1000 deg^2, chosen to sample a similar volume to the SDSS luminous red galaxy sample. The total number of galaxies is 8.7×10^5. To ensure sufficient resolution on the variations of $D_A(z)$ and $H(z)$, we subdivide the $z \sim 1$ survey into four redshift bins centering at $z = 0.6$, 0.8, 1.0, and 1.2 with widths $\Delta z = 0.2$. Hereafter, unless noted, the term "$z \sim 1$ survey" designates the sum of these four redshift bins.

For the nearby universe, we adopt the parameters of the ongoing SDSS luminous red galaxy survey (Eisenstein et al. 2001). The survey volume for this sample is $1\ h^{-3}$ Gpc^3, and the comoving number density is $10^{-4}\ h^3$ Mpc^{-3} at $z \approx 0.3$. This survey is included in all analyses in this paper because it is well underway. We use $\sigma_{8,g} = 1.8$ for these galaxies.

To resolve the oscillations along the line of sight at $k \approx 0.2\ h$ Mpc^{-1}, and thereby measure $H(z)$, requires that the position of the galaxy along the line of sight be well estimated. As the crest-to-trough distance for this wavelength is only 15 h^{-1} Mpc, we need redshifts with accuracy of about 10^{-3} in $1 + z$. We return to this computation in § 4.5, but for now we note that this accuracy requires low-resolution spectroscopy. Photometric redshifts cannot recover $H(z)$ from the acoustic oscillations.

4. RESULTS AND DISCUSSION

4.1. *Redshift Surveys with SDSS and CMB*

We begin by presenting the results for cosmography from our baseline surveys. Table 3 lists the errors on $D_A(z)$ and $H(z)$ for a combination of all the baseline redshift surveys

TABLE 3

MARGINALIZED ERRORS ON $D_A(z)$ AND $H(z)$ FOR ΛCDM

Redshift	$D_A(z)$ (%)	$H(z)$ (%)
0.3	5.19	5.80
0.6	4.30	5.19
0.8	3.22	3.59
1.0	2.30	2.84
1.2	2.03	2.53
3	1.19	1.48
1000	0.219	...

NOTE.—The fractional percentage errors (1 σ) on cosmological distances from the combination of CMB, SDSS, and our standard surveys at $z \sim 1$ and $z = 3$.

and the CMB data. The errors improve at higher redshift because of the smaller scale of the nonlinear contamination. At $z = 3$, the constraints are particularly good, better than 2% on both quantities. The errors on $D_A(z)$ are generally smaller than those on $H(z)$. This is simply because the number of modes available in the two transverse directions is bigger than the number of modes in the one line-of-sight direction.

The reduced covariance matrix of the $D_A(z)$ and $H(z)$ values is shown in Table 4. $D_A(z)$ and $H(z)$ at different redshifts are covariant only through the uncertainty in the physical scale of the acoustic oscillations. From the tiny nondiagonal terms between different redshift bins in Table 4, we can see that the sound horizon scale is very well determined. The nondiagonal elements of $D_A(z)$ and $H(z)$ in the same redshift bin show that the degeneracy between the two is indeed small as they are determined independently by the standard ruler test.

Most of the behavior in the errors can be explained as variations in the nonlinear cutoff scale $k_{\rm max}$ and in the survey sizes $V_{\rm survey}$. We explore this in Figure 4 by showing how the performance at $z = 1$ depends on $k_{\rm max}$. In the left-hand panel of Figure 4 we plot the errors on D_A and H as functions of $k_{\rm max}$ for two values of the number density n. The drop from $k_{\rm max} = 0.1$ to $0.2\,h\,{\rm Mpc}^{-1}$ dominates the increase in performance from $z = 0.3$ to 1.2.

The errors on the distances flatten at around $k_{\rm max} \sim 0.25\,h\,{\rm Mpc}^{-1}$, implying a saturation of the information from the locations of baryonic acoustic peaks. This is easily understood as the drop in contrast of the higher harmonics because of Silk damping. Beyond this wavenumber, the errors slowly decrease with more efficiency for $H(z)$. This slight increase in information seems to be due to the Alcock-Paczynski effect reappearing as the deviation of the power spectrum from a pure power law is revealed by the increasing range of wavenumbers in the survey.

The oscillatory behavior versus $k_{\rm max}$ shown in the left-hand panel of Figure 4 is due to the oscillatory derivatives of the power spectrum with respect to dilations in the distance scales. When $k_{\rm max}$ is close to the nodes of power spectrum, the derivative $d\ln P/d\ln k$ has a local maximum and the survey can better distinguish the differing cosmologies. The right-hand panel of Figure 4 shows the covariance between the uncertainties in $D_A(z)$ and $H(z)$. These show a similar dependence on $d\ln P/d\ln k$, but with a phase offset. When the performance improves rapidly, the ability to separate the two distances has a local maximum. Thus, the decrease of the nondiagonal term at $z = 1$ and 1.2 in Table 4 is simply because $k_{\rm max}$ has shifted to be near one of the maxima of the plot in the right-hand panel of Figure 4. The increasing covariance between $D_A(z)$ and $H(z)$ at very large $k_{\rm max}$ is another signature of the Alcock-Paczynski effect in the broadband power that eventually intrudes.

Figure 4 also shows the degradation of performance caused by shot noise. We generate results with essentially zero shot noise by increasing the galaxy number density by a factor of 100. This reveals the bare effect of $k_{\rm max}$ variations; with the baseline surveys, the power spectrum errors at large k are somewhat degraded by increasing shot noise. The left-hand panel of Figure 4 displays the ratio of performance in the two cases. For $k \approx 0.2\,h\,{\rm Mpc}^{-1}$, the degradation due to shot noise is less than a factor of 1.5, as expected. However, at large k, the effect is a full factor of 2. Improved performance at large k increases the strength of the Alcock-Paczynski effect, as shown by the even larger covariance in the high density case in the right-hand panel.

We next project the errors from the baseline surveys through to constraints on the dark energy parameters. Table 5 shows the performance on dark energy parameters using fiducial model 1 (ΛCDM). With all redshift surveys combined with CMB and SDSS data, we can achieve a precision of 0.037 on Ω_X, 0.25 on $w(z = 0)$, 0.10 on $w(z = 0.8)$,

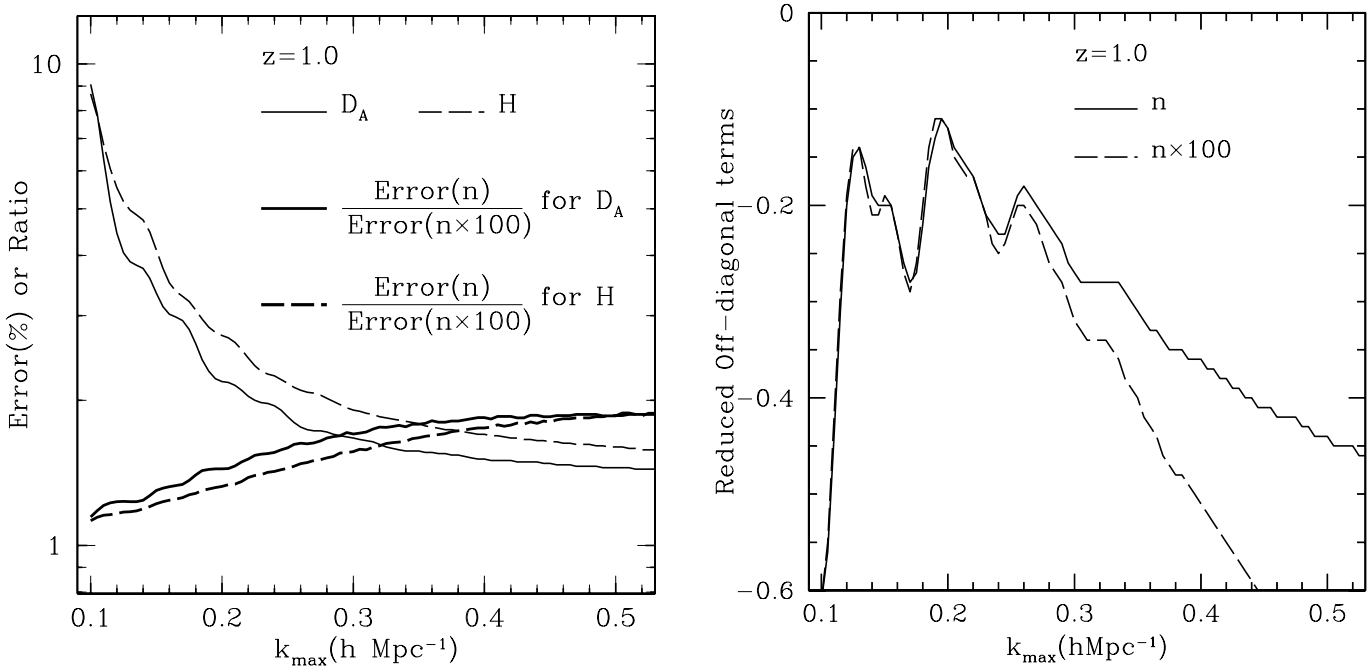

FIG. 4.—Errors on $D_A(z)$ and $H(z)$ as a function of $k_{\rm max}$ and n for the $z = 1$ bin. Here n means the baseline number density in Table 1 ($5 \times 10^{-4}\,h^3\,{\rm Mpc}^{-3}$) and $n \times 100$ means 100 times the baseline number density.

TABLE 4

CORRELATION MATRIX FOR DISTANCE MEASUREMENTS IN ΛCDM

		CMB	$z = 0.3$		$z = 0.6$		$z = 0.8$		$z = 1.0$		$z = 1.2$		$z = 3.0$	
z	PARAMETER	D_A	D_A	H	D_A	H	D_A	H	D_A	H	D_A	H	D_A	H
	$D_{ii}^{1/2}$[a]	0.002	0.052	0.058	0.043	0.052	0.032	0.036	0.023	0.028	0.020	0.025	0.012	0.015
CMB.....	D_A	1.000	0.040	−0.048	0.054	−0.045	0.061	−0.064	0.103	−0.087	0.123	−0.100	0.233	−0.192
0.3.....	D_A	0.040	1.000	−0.256	0.002	−0.002	0.003	−0.003	0.005	−0.004	0.006	−0.005	0.011	−0.009
	H	−0.048	−0.256	1.000	−0.003	0.003	−0.003	0.004	−0.006	0.005	−0.007	0.006	−0.013	0.011
0.6.....	D_A	0.054	0.002	−0.003	1.000	−0.255	0.004	−0.004	0.006	−0.005	0.008	−0.006	0.015	−0.012
	H	−0.045	−0.002	0.003	−0.255	1.000	−0.003	0.003	−0.005	0.005	−0.006	0.005	−0.012	0.010
0.8.....	D_A	0.061	0.003	−0.003	0.004	−0.003	1.000	−0.304	0.007	−0.006	0.009	−0.007	0.016	−0.013
	H	−0.064	−0.003	0.004	−0.004	0.003	−0.304	1.000	−0.008	0.006	−0.009	0.007	−0.017	0.014
1.0.....	D_A	0.103	0.005	−0.006	0.006	−0.005	0.007	−0.008	1.000	−0.124	0.015	−0.012	0.028	−0.023
	H	−0.087	−0.004	0.005	−0.005	0.005	−0.006	0.006	−0.124	1.000	−0.012	0.010	−0.024	0.020
1.2.....	D_A	0.123	0.006	−0.007	0.008	−0.006	0.009	−0.009	0.015	−0.012	1.000	−0.120	0.033	−0.028
	H	−0.100	−0.005	0.006	−0.006	0.005	−0.007	0.007	−0.012	0.010	−0.120	1.000	−0.027	0.023
3.0.....	D_A	0.233	0.011	−0.013	0.015	−0.012	0.016	−0.017	0.028	−0.024	0.033	−0.027	1.000	−0.203
	H	−0.192	−0.009	0.011	−0.012	0.010	−0.013	0.014	−0.023	0.020	−0.028	0.023	−0.203	1.000

NOTE.—All terms are normalized by diagonal terms given in the first row: $a'_{ij} = a_{ij}/(a_{ii}a_{jj})^{1/2}$.

[a] The square root of the diagonal terms of the covariance matrix. These are the 1 σ fractional percentage errors on these quantities.

TABLE 5
MARGINALIZED ERRORS ON DARK ENERGY PARAMETERS FOR ΛCDM

$z \sim 1$	$z = 3$	SNe	$\sigma_{\Omega_m h^2}/\Omega_m h^2$	σ_{Ω_x}	σ_{w_0}	σ_{w_1}	$z_{\rm pivot}$	$\sigma_{w_{z,\rm pivot}}$
			0.0094	0.0926	0.882	1.172	0.729	0.218
Y			0.0090	0.0378	0.281	0.353	0.735	0.107
	Y		0.0086	0.0758	0.466	0.446	0.959	0.184
Y	Y		0.0083	0.0368	0.245	0.280	0.796	0.102
		Y	0.0093	0.0088	0.116	0.231	0.478	0.035
Y		Y	0.0088	0.0083	0.093	0.183	0.471	0.033
	Y	Y	0.0086	0.0085	0.096	0.189	0.479	0.034
Y	Y	Y	0.0082	0.0082	0.083	0.161	0.476	0.032

NOTES.—"Y" indicates the data sets being used; CMB and SDSS data are included in all sets. The baseline redshift survey parameters (V1N1) are used (Table 1). The value $z_{\rm pivot}$ is the redshift at which the errors on the value of $w(z)$ are independent from the slope w_1. The value $\sigma(w_{z,\rm pivot})$ is the error on the value of w at that redshift; this is also the error on w that would be found if w_1 were held fixed at the fiducial value. All errors are 1 σ.

and 0.28 on w_1. For the ΛCDM model, as well as for model 2 in Table 2, we did not clip w_1 for $z > z_t$ with $z_t = 2$. Clipping w_1 for $z > z_t$ in ΛCDM increases the errors by a factor of 1.2.

In these calculations we assumed not only that the errors on the distances were Gaussian but also that these generate a Gaussian likelihood function for the dark energy parameters. This is appropriate for well-constrained parameters such as distances, Ω_X, and $\Omega_m h^2$ but may be incorrect for w_0 and w_1. We repeated our analysis with a more complete likelihood calculation, in which the likelihood at each point in w_0-w_1 space was computed assuming a (more appropriate) Gaussian likelihood in the other parameters. The result is the likelihood function in w_0 and w_1 with the other parameters marginalized out. The resulting likelihood contours were not ellipsoids, of course, and were slightly bent and offset. However, the extent and slope of the contours were excellent matches to the Gaussian ellipsoids. We therefore conclude that the Gaussian analysis gives a reasonable estimate of the dark energy performance and is sufficient for comparing different combinations of surveys.

Constraints on dark energy fiducial models 2–6 are presented in Table 6. Some of these non-ΛCDM models have significantly improved performance on dark energy parameters. In particular, models 2 ($w = -\frac{2}{3}$) and 3 ($w_0 = -\frac{2}{3}$, $w_1 = \frac{1}{6}$) have superb performance, with constraints on w_1 reaching 9%. Models 4 and 6 are also better than ΛCDM. Not surprisingly, these improvements correlate directly with the value of w at intermediate redshifts and hence with the amount of dark energy that remains at that time. Thus, most improvements are keyed by the measurement of $H(z)$ and $D_A(z)$ at higher redshifts. This is reflected in the systematic increase of $z_{\rm pivot}$ in the cases of improved performance.

4.2. *Incorporation of Supernova Data*

We next combine these redshift surveys with the SN data set. The lower four rows of Table 5 show the error on dark energy parameters with the SN survey. To begin, SN data with only CMB and SDSS data yield impressive performance. Ω_X and w_0 are well constrained, and the error on w_1 is 0.23, slightly better than what the redshift surveys produce. When we combine the SN data with the galaxy redshift surveys, the w_1 error improves to 0.16. With the SN and CMB data, the inclusion or exclusion of SDSS does not change the result much because of the relatively large uncertainty in both $H(z)$ and $D_A(z)$ from SDSS as compared to the performance of SNe; most of the information in the survey is superseded by SN data.

Figure 5 shows the constraints in the w_0-w_1 plane as error ellipses, marginalizing over all other parameters. The left-hand panel shows the ΛCDM model, and the right-hand panel shows model 2 ($w = -\frac{2}{3}$) as a comparison to ΛCDM. We see the difference in the directions of the two ellipses: SNe with CMB and SDSS, and redshift surveys with CMB and SDSS. The set with SNe shows a tight constraint especially in the w_0 direction and the improvement of the constraint on w_1 by redshift surveys. By comparing two models, we can easily see that model 2 allows much better constraints on parameters than ΛCDM and favors redshift surveys more. The redshift survey data are now comparable to the capability of SNe: in w_1, redshift survey data achieve 0.08, SN survey data produce 0.12, and together the data sets produce 0.05 (Table 6).

The SN data have superb precision for $z < 1.7$ in $D_A(z)$ and give excellent constraints on the shape of the distance-redshift relation. Our baseline redshift surveys, on the other hand, have larger error bars than SNe for $z \leq 1.2$, but they have an advantage of having a distance-redshift data point at very high redshift ($z = 3$) and measuring $H(z)$ in all redshift bins. In the ΛCDM fiducial model, the contributions to w_1 by $H(z)$ measurements and $D_A(z)$ from the $z = 3$ redshift survey are slightly less useful than the good precision of $D_A(z)$ from SNe at lower redshifts (see Fig. 3). On the other hand, dark energy models with more positive w have larger signatures at higher redshift. This is good for both data sets but helps the redshift surveys more.

4.3. *Variation with Redshift Survey Parameters*

We next show how performance varies with survey parameters such as the total number of galaxies N and survey volume ($V_{\rm survey}$). We present variations in $V_{\rm survey}$ and N by factors of 5 in Table 7. Because the cosmographic performance in each redshift survey is essentially independent, one can interpret this table as varying each survey independently. The SDSS and CMB data are unchanged in all cases. From Table 7, we can see that performance at $z = 3$ is more sensitive to the increase in N at fixed $V_{\rm survey}$ (i.e., higher target density) than for the reverse. For the $z \sim 1$ surveys, the effect of increasing the number density is slightly larger for $z = 1.0$ and 1.2 bins and is more efficient for $D_A(z)$ than for

TABLE 6

COSMOLOGICAL ERRORS FROM DIFFERENT FIDUCIAL DARK ENERGY MODELS

Model	$z \sim 1$	$z = 3$	SNe	$\sigma_{\Omega_m h^2}/\Omega_m h^2$	σ_{Ω_x}	σ_{w_0}	σ_{w_1}	$z_{\rm pivot}$	$\sigma_{w_{z,\rm pivot}}$
2.....	Y			0.0090	0.0259	0.129	0.092	1.249	0.057
		Y		0.0088	0.0485	0.247	0.158	1.484	0.078
	Y	Y		0.0085	0.0245	0.119	0.081	1.333	0.050
			Y	0.0094	0.0134	0.087	0.122	0.682	0.023
	Y		Y	0.0090	0.0088	0.049	0.062	0.714	0.022
		Y	Y	0.0087	0.0097	0.056	0.072	0.713	0.023
	Y	Y	Y	0.0084	0.0083	0.045	0.052	0.744	0.022
3.....	Y			0.0090	0.0266	0.131	0.097	1.306	0.033
		Y		0.0088	0.0530	0.268	0.190	1.389	0.043
	Y	Y		0.0085	0.0256	0.124	0.089	1.351	0.028
			Y	0.0094	0.0158	0.081	0.107	0.741	0.019
	Y		Y	0.0090	0.0092	0.045	0.049	0.853	0.017
		Y	Y	0.0087	0.0103	0.051	0.058	0.821	0.018
	Y	Y	Y	0.0085	0.0086	0.042	0.042	0.906	0.016
4.....	Y			0.0090	0.0320	0.180	0.144	1.203	0.049
		Y		0.0088	0.0653	0.367	0.275	1.314	0.065
	Y	Y		0.0085	0.0313	0.171	0.132	1.259	0.043
			Y	0.0094	0.0127	0.106	0.142	0.729	0.022
	Y		Y	0.0090	0.0090	0.062	0.075	0.774	0.021
		Y	Y	0.0087	0.0098	0.070	0.087	0.764	0.022
	Y	Y	Y	0.0085	0.0086	0.056	0.064	0.803	0.021
5.....	Y			0.0090	0.0454	0.353	0.429	0.773	0.122
		Y		0.0086	0.0844	0.560	0.547	0.968	0.183
	Y	Y		0.0083	0.0443	0.312	0.344	0.846	0.113
			Y	0.0094	0.0089	0.132	0.258	0.488	0.040
	Y		Y	0.0089	0.0085	0.106	0.206	0.480	0.038
		Y	Y	0.0086	0.0087	0.109	0.208	0.491	0.038
	Y	Y	Y	0.0083	0.0084	0.095	0.179	0.487	0.037
6.....	Y			0.0090	0.0368	0.240	0.232	0.975	0.078
		Y		0.0087	0.0766	0.463	0.386	1.166	0.107
	Y	Y		0.0084	0.0365	0.224	0.201	1.057	0.070
			Y	0.0094	0.0101	0.119	0.190	0.604	0.029
	Y		Y	0.0090	0.0086	0.081	0.125	0.609	0.029
		Y	Y	0.0087	0.0090	0.087	0.133	0.619	0.028
	Y	Y	Y	0.0084	0.0084	0.071	0.105	0.626	0.028

NOTES.—"Y" indicates the data sets being used; CMB and SDSS data are included in all sets. The baseline redshift survey parameters (V1N1) are used.

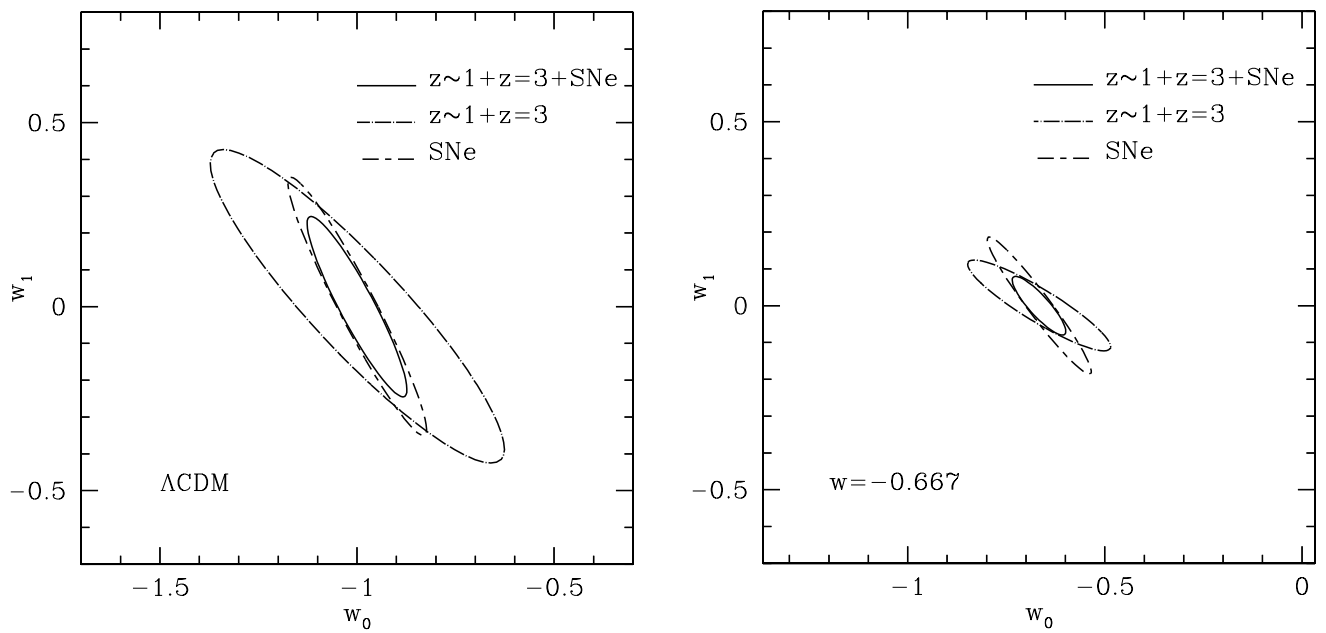

FIG. 5.—Elliptical error regions on w_0 and w_1 for two different fiducial models. All other parameters have been marginalized over, and the contours are for 68% likelihood. CMB and SDSS are included in all cases.

TABLE 7

MARGINALIZED ERRORS ON $D_A(z)$ AND $H(z)$ AS A FUNCTION OF SURVEY PARAMETERS

SURVEYS			REDSHIFT					
$z \sim 1$	$z = 3$	PARAMETER	0.3	0.6	0.8	1.0	1.2	3.0
V1N1	V1N1	$D_A(z)$	5.19	4.30	3.22	2.30	2.03	1.19
		$H(z)$	5.80	5.19	3.59	2.84	2.53	1.48
V1N5	V1N5	$D_A(z)$	5.19	3.50	2.57	1.74	1.52	0.88
		$H(z)$	5.80	4.44	3.00	2.30	2.01	1.08
V5N1	V5N1	$D_A(z)$	5.19	3.52	2.75	2.12	1.91	1.10
		$H(z)$	5.80	3.83	2.79	2.32	2.13	1.33
V5N5	V5N5	$D_A(z)$	5.19	1.93	1.45	1.04	0.93	0.57
		$H(z)$	5.80	2.33	1.62	1.28	1.15	0.69

NOTES.—1 σ fractional percentage errors on cosmological distances. CMB and SDSS are included in all sets. For SDSS, the baseline survey parameters (V1N1) are always used. V5N1: 5 times larger survey volume with 5 times smaller number density. V1N5: 5 times higher number of objects with the baseline survey volume, i.e., 5 times higher number density. V5N5: 5 times more survey volume with the baseline number density.

$H(z)$. Increasing $V_{\rm survey}$ was more effective for $z = 0.6$ and 0.8 bins with a general trend of being more efficient for $H(z)$ than for $D_A(z)$. This agrees with the result from Table 1 that the nP values of $z = 1.0$ and 1.2 are somewhat less than those of $z = 0.6$ and 0.8. The preference to $H(z)$ when decreasing the number density is a result of an increased contribution from wavevectors along the line of sight, which suffer less shot-noise degradation as a result of their enhanced amplitude from redshift distortions.

The projected errors on the dark energy parameters under these various survey parameters are presented in Table 8. The results are consistent with the changes in the errors on $D_A(z)$ and $H(z)$. The graphical illustrations of these errors are shown by error ellipses in Figure 6. For this figure, the surveys at $z \sim 1$ (*left-hand panel*) and $z = 3$ (*right-hand panel*) are used separately so that one can see the individual scalings. As one would expect, larger surveys provide better constraints. The slopes of the major axes are an indicator of the typical redshift $z_{\rm pivot}$ of the data. The twisting of the major-axis direction in the $z = 3$ case is a visual sign that larger $z = 3$ surveys pull $z_{\rm pivot}$ to be higher than the CMB and SDSS data would yield by themselves.

As regards the survey size, increasing $V_{\rm survey}$ at fixed number density causes the performance to scale nearly as the square root of $V_{\rm survey}$. In detail, the results fall slightly short of this scaling because the SDSS and CMB data are not similarly scaled. With a factor of 5 size increase in the $z = 3$ survey, one begins to see the limitations of the CMB calibration of the sound horizon.

When combined with the SN data, it is more valuable to improve the $z = 3$ survey than the $z \sim 1$ survey. Increasing $V_{\rm survey}$ by a factor of 5 (V5N5) for both surveys improves the errors on w_1 by a factor of 1.6, increasing the $z \sim 1$ surveys alone yields a 1.3 improvement, whereas increasing $z = 3$ alone improves by a factor of 1.4. Pictorially, this is because the $z = 3$ constraint ellipsoids for dark energy fall at more of an angle as compared to the SN ellipsoids than do the $z \sim 1$ ellipsoids. Physically, it is more advantageous to widen the redshift range of the measurements, especially because the SN data have somewhat higher precision than the $z \sim 1$ redshift survey constraints on $D_A(z)$.

As mentioned in § 3.5, adjusting the survey volume $V_{\rm survey}$ while holding the total number of targets fixed has an optimum point for the measurement of the power spectrum at $nP = 1$. We therefore expect that this trend would extend to performance on dark energy parameters. Indeed, we find that slightly larger surveys (e.g., a factor of 2–3) do give small improvements and that much larger surveys give steadily worse performance. Again, this is exactly as we expected with our choice to aim for $nP \approx 3$. True optimization of course requires detailed knowledge of the survey instrument, the source population, the possible systematic errors, and the other science goals of the survey.

TABLE 8

MARGINALIZED ERRORS FOR ΛCDM FOR VARIOUS SURVEY SIZES

$z \sim 1$	$z = 3$	$\sigma_{\Omega_m h^2}/\Omega_m h^2$	σ_{Ω_x}	σ_{w_0}	σ_{w_1}	$z_{\rm pivot}$	$\sigma_{w_{z,\rm pivot}}$
V1N1		0.0090	0.0378	0.281	0.353	0.735	0.107
V5N5		0.0079	0.0195	0.142	0.191	0.680	0.056
	V1N1	0.0086	0.0758	0.466	0.446	0.959	0.184
	V5N5	0.0070	0.0724	0.399	0.306	1.239	0.126
V1N1	V1N1	0.0083	0.0368	0.245	0.280	0.796	0.102
V1N1	V5N5	0.0069	0.0358	0.210	0.199	0.961	0.088
V5N5	V1N1	0.0074	0.0192	0.135	0.176	0.699	0.055
V5N5	V5N5	0.0064	0.0186	0.120	0.142	0.762	0.053

NOTES.—Left two columns indicate how the sizes of the $z \sim 1$ and $z = 3$ surveys are being varied; blanks mean that the survey is excluded. CMB and SDSS are included in all rows. For SDSS, the baseline survey parameters (V1N1) are always used.

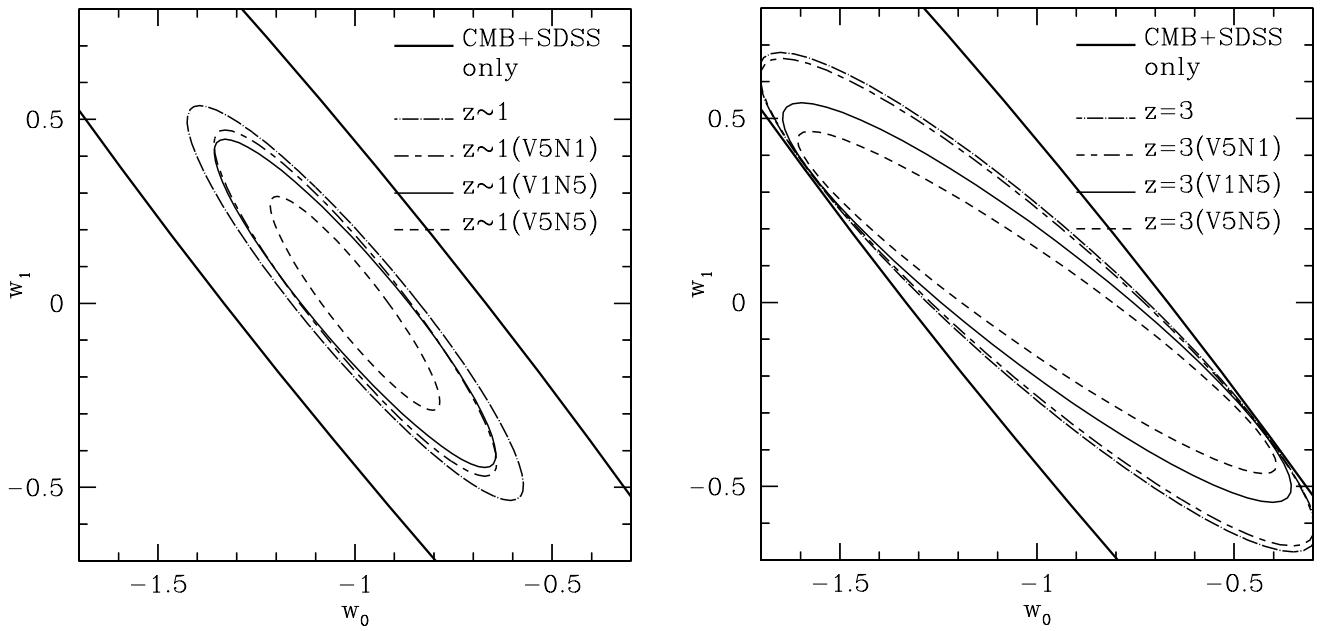

FIG. 6.—Elliptical error regions on w_0 and w_1 as a function of survey parameters (ΛCDM). All other parameters have been marginalized over, and the contours are for 68% likelihood. CMB and SDSS are included in all cases. V5N1 means 5 times the baseline survey volume with 5 times smaller number density. V1N5 means 5 times the baseline number density. V5N5 means 5 times the baseline survey volume with the baseline number density. The ellipse with no notation on survey parameters means the baseline survey parameters. For SDSS, the baseline survey parameters were used in all cases.

4.4. *Baryonic Oscillations versus Broadband Constraints*

To this point, we have discussed the baryonic oscillations as a distinct signature from which to infer cosmological distances. Although these features are essential, the Fisher matrix we calculate includes additional contributions such as the overall broadband shape of the power spectrum. In this section we briefly assess the amount of information on distances from baryonic oscillations apart from other contributions.

To single out the nonbaryonic contribution, we repeat our calculations with a fiducial model with 10 times lower baryon fraction ($\Omega_b = 0.005$), thereby removing the acoustic oscillations from the power spectrum. Overall, the errors on $D_A(z)$ and $H(z)$ increase by a factor of 2–3, with more increase in the $z \sim 1$ set and more increase in $D_A(z)$ than $H(z)$, making the magnitudes of $\sigma_{D_A}(z)$ and $\sigma_H(z)$ nearly equal. The reduced correlation coefficient between $D_A(z)$ and $H(z)$ at the same redshift is about -0.8, indicating a strong correlation. This covariance and the more equal precisions imply that the Alcock & Paczynski (1979) test (hereafter AP test) is playing a significant role in constraining distances in the low-baryon case. The combination $D_A H$ is well constrained, whereas the separate values of $D_A(z)$ and $H(z)$ are constrained only by the broadband shape of the power spectrum.

The AP effect can isolate cosmological distortions in two ways. First, when the power spectrum has a preferred scale (and any deviation from a power law will suffice), we can measure the cosmological distortion $D_A H$ by requiring that scale to be isotropic. The values of $D_A(z)$ and $H(z)$ can be determined separately only if the preferred scale is known, for example, from CMB data. Second, one can attempt to separate the cosmological distortions from the redshift distortions by the angular dependence of the power spectrum at a given k. When the redshift distortion is weak ($\beta \approx 0$), the two distortions have identical angular signatures, both quadratic in μ, and hence are indistinguishable. However, for larger β, both distortions take on more complicated forms that lift the degeneracy in principle.

Because in our analysis the shape of the power spectrum is known from the CMB data, the first mode of the AP effect cannot produce the strong covariance between $D_A(z)$ and $H(z)$ that we find in the $\Omega_b = 0.005$ case. Hence, the degeneracy between the redshift distortions and the cosmological distortions must be angularly broken (i.e., the second mode of the AP effect). To test this, we introduce a strong degeneracy between $D_A H$ and β by using $\beta \approx 0$. For numerical reasons, we decrease the fiducial β-values 30-fold. We apply these lower β-values only to the computations of the derivatives; the original β-values are retained in computing $V_{\rm eff}$ so that the weighting of the radial and tangential modes is unchanged. The upper two rows in Table 9 show the results with $\Omega_b = 0.005$. With negligible β-values, the errors increase by 15%–35% compared to the case with the normal β-values, with more increase for $D_A(z)$ than $H(z)$ and more increase in the $z \sim 1$ set, which has larger β than the others.

TABLE 9
MARGINALIZED ERRORS ON $D_A(z)$ AND $H(z)$ WITH NEGLIGIBLE β FOR DIFFERENT BARYON FRACTIONS

		REDSHIFT					
Ω_b	PARAMETER	0.3	0.6	0.8	1.0	1.2	3.0
0.005.....	$D_A(z)$	13.03	15.64	11.47	9.21	7.68	3.16
	$H(z)$	12.71	14.05	10.50	8.49	7.27	3.56
0.05.....	$D_A(z)$	5.80	5.66	4.03	2.92	2.59	1.44
	$H(z)$	6.68	7.83	4.75	4.04	3.64	2.03

NOTES.—1 σ fractional percentage errors on cosmological distances for ΛCDM. CMB and SDSS are included in all sets. The derivatives are computed with $\beta \approx 0$, thereby causing the redshift and cosmological distortions to be more degenerate. The usual β-values are used to compute $V_{\rm eff}$.

The reduced correlation coefficients decrease to roughly -0.3, supporting the interpretation that the AP effect has been removed and the remaining constraints are due to the shape of the broadband power spectrum.

We next apply the same method for the $\Omega_b = 0.05$ case so as to enforce degeneracy between the cosmological and redshift distortions. The lower half of Table 9 shows the errors on distances in this case. The comparison between the $\Omega_b = 0.05$ and $\Omega_b = 0.005$ cases in Table 9 shows that the broadband spectrum is a minor effect compared to the baryonic oscillations. Comparing these results to the previous results in Table 3 shows that the performance from the baryonic oscillations will decrease by 10%–50% if we assume that we do not know the behavior of the redshift distortions very well.

To summarize, in the absence of baryonic oscillations, the AP effect is capable of constraining the combined quantity $D_A H$ very well provided that the shape of the redshift distortions is relatively well known (Ballinger et al. 1996; Heavens & Taylor 1997; Hatton & Cole 1999; Taylor & Watts 2001; Matsubara & Szalay 2002, 2003). However, it is the baryonic oscillations that separate $D_A(z)$ and $H(z)$ most effectively and provide precision constraints regardless of the amount of information on the redshift distortions.

4.5. *Photometric Redshift Surveys*

With the advent of deep wide-field multicolor imaging surveys, it is natural to ask whether photometric redshifts can be used for studies of the acoustic oscillations. In this section we study how uncertainties in the galaxy redshifts affect our results. There are two basic lessons. First, recovering the Hubble parameter $H(z)$ requires measuring clustering on fairly small scales along the line of sight, so that redshift precision substantially better than 1% is needed. Second, redshift slices selected with photometric redshifts can be sufficiently thin that the acoustic oscillations survive in the angular power spectrum. This means that one can measure $D_A(z)$ with these surveys, albeit with worse precision per unit survey sky coverage. Hence, photometric redshift surveys lose the advantage of the acoustic oscillations to measure $H(z)$ directly but could measure $D_A(z)$ if one has a large enough survey. The idea of using transverse clustering to probe dark energy was analyzed in the weak-lensing context by Cooray et al. (2001).

When redshifts are uncertain, one is smearing together clustering at multiple distances along the line of sight. Our first task is to consider whether the acoustic oscillations, being narrow features in Fourier space, can survive this projection. The controlling effect is the variation in the comoving angular diameter distance across the range of redshift uncertainty. This can be addressed with Limber's equation (Limber 1953; Baugh & Efstathiou 1994). We model the redshift distribution as a Gaussian of width σ_z and consider the effects on the angular power spectrum. This is shown in Figure 7, where we plot the derivative $d\ln P/d\ln k$ that controls the measurement of cosmological distortions for three different values of σ_z. We adopt a $z = 1$ slice and consider 0%, 4%, and 8% uncertainties ($1\,\sigma$) in $1 + z$. One can see that the oscillation pattern is essentially intact at 4% but substantially degraded at 8%. In detail, we estimate that the errors on $D_A(z)$ would be increased by 13% for the 4% case and 54% for the 8% case. The effects at $z = 3$ are slightly more forgiving, despite the higher $k_{\max}$ and hence narrower features, because the derivative of $D_A(z)$ versus z is slightly less. We therefore conclude that photometric redshift errors of 4% in $1 + z$ ($1\,\sigma$) are sufficient to preserve the acoustic oscillations for the measurement of $D_A(z)$ at $z \gtrsim 0.5$.

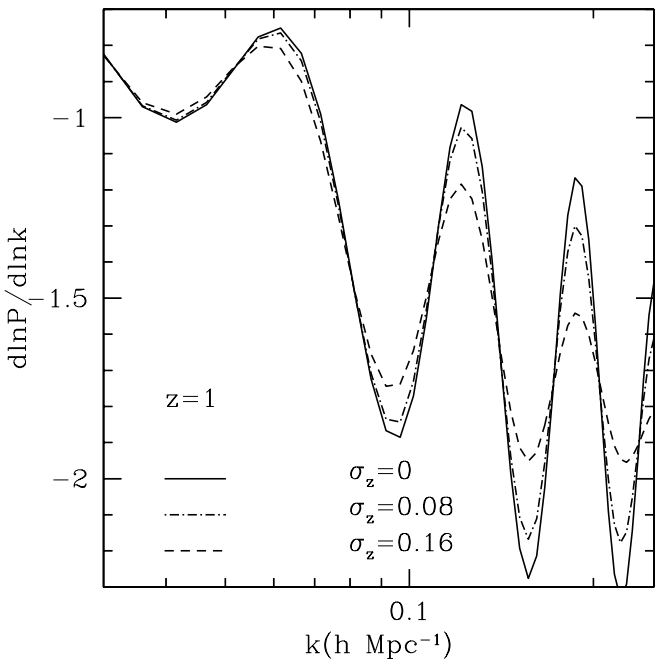

FIG. 7.—Derivative $d\ln P/d\ln k$ as a function of wavenumber for three different values of the redshift uncertainty. Larger uncertainties cause line-of-sight projections that smear the narrow acoustic oscillations and impede the detectability of cosmological distortions. Here $\sigma_z = 0.0$ represents spectroscopic redshift error, whereas $\sigma_z = 0.08$ and 0.16 correspond to 4% and 8%, respectively, of $\sigma_z/(1+z)$ at $z = 1$. [*See the electronic edition of the Journal for a color version of this figure.*]

Having found that the transverse power spectrum is not affected by reasonable projections, we next include the redshift uncertainty in our Fisher matrix formalism. We do this by retaining the Euclidean approximation, i.e., treating the survey as a box of fixed D_A and H, but smearing the radial position by a Gaussian uncertainty. If the line-of-sight comoving position r_z is convolved with an uncertainty of the form $\exp[-(\Delta r_z)^2/2\sigma_r^2]$ with an uncertainty σ_r, then the Fourier transform of the density field will simply be diminished by the transform of this kernel: $\delta_{\boldsymbol{k}} \propto \exp(-k_\parallel^2\sigma_r^2/2)$. The observed power spectrum is then (L. Hui 2000, private communication)

$$P(\boldsymbol{k}) = P_{\rm obs}(\boldsymbol{k}) e^{-k_\parallel^2\sigma_r^2}\ , \tag{18}$$

where $P_{\rm obs}$ was given in equation (14). In other words, the power is strongly suppressed for large $k_\parallel$. The positional uncertainty is related to the redshift uncertainty σ_z by $\sigma_r = c\sigma_z/H(z)$.

The introduction of this suppression enters the Fisher matrix calculation through its effect on the effective volume. Modes with a relatively large $k_\parallel$ will be swamped by shot noise and therefore give no leverage on the power spectrum measurements. Only modes with $k_\parallel\sigma_r \lesssim 1$ are useful. Much lower shot noise allows one to retain modes of larger $k_\parallel$, but one is fighting a Gaussian suppression.

Because the measurement of $H(z)$ depends on modes aligned near the line of sight, the suppressed contribution from modes with large $k_\parallel$ increases the error on $H(z)$

significantly. The measurement of $D_A(z)$ arises from more transverse modes, and modes with $k_\parallel = 0$ always exist to give some measurement of $D_A(z)$. However, for large k, only a thin slab of modes with $k_\parallel \lesssim 1/\sigma_r$ remains useful. As the number of modes will scale as σ_r^{-1}, we expect that the errors on $D_A(z)$ will scale as $\sigma_r^{1/2}$ for $k_{\max}\sigma_r \gg 1$.

Figure 8 shows the fractional errors on $H(z)$ and $D_A(z)$ as a function of σ_r for redshift surveys at $z = 1.0$ and 3. The errors are constant for small σ_r and then increase rapidly beyond a characteristic threshold. Performance at $z = 3$ degrades at smaller σ_r than performance at $z = 1.0$. This is because of the larger value of $k_{\max}$ for $z = 3$. An additional small but nonzero effect is that the redshift distortions are smaller at $z = 3$ than at $z = 1$. Larger distortions increase the power in the radial direction and allow modes with slightly larger $k_\parallel$ to survive the shot noise. The errors on $H(z)$ degrade sharply for $\sigma_r \gtrsim 10\,h^{-1}$ Mpc at $z = 1$ and $5\,h^{-1}$ Mpc at $z = 3$. These correspond to redshift errors σ_z of 0.006 and 0.007, respectively. In terms of wavelength resolution σ_λ/λ, these are 0.003 and 0.002. Hence, our general result is that fractional errors of 0.25% in $1 + z$ are required to recover $H(z)$.

In Figure 8, the errors on $D_A(z)$ in both redshift bins increase relatively slowly at $\sigma_r \gtrsim 10\,h^{-1}$ Mpc and achieve the predicted $\sigma_r^{1/2}$ dependence at large σ_r. Therefore, to calculate σ_{D_A} with σ_r bigger than the values appearing in Figure 8, we can use $\sigma_r^{1/2}$ dependence to interpolate [up to the limit of $\sigma_z/(1 + z) \approx 4\%$]. For numerical reasons, we assume a redshift error of 1% in photometric redshift. This is too optimistic for a normal photometric redshift, but one can scale to larger uncertainties. For example, a 4% uncertainty would have errors twice as large, which could be compensated by making the survey area 4 times as large. The 1% errors in $(1 + z)$ correspond to $\sigma_r = 34\ h^{-1}$ Mpc at $z = 1$ and $\sigma_r = 27\,h^{-1}$ Mpc at $z = 3$.

Table 10 shows the errors on $D_A(z)$ and $H(z)$ for different survey conditions. Increasing the survey volume fivefold while keeping the target density fixed (i.e., V5N5) decreases the error by $\sim\sqrt{5}$, as before. Further increases of the survey volume, which are omitted in Table 10, continue to follow the simple trend of $V_{\rm survey}^{1/2}$. Increasing the number density with fixed $V_{\rm survey}$ is slightly more efficient than the spectroscopic redshift case ($\sigma_r = 0$) because the exponential suppression of modes with nonzero $k_\parallel$ means that there are always modes that benefit from a larger n to achieve $nP \sim 1$.

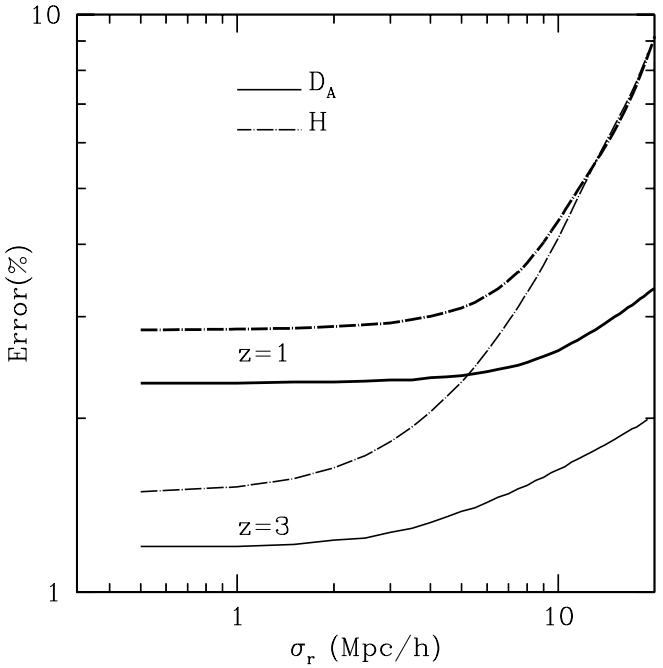

FIG. 8.—Error on $D_A(z)$ and $H(z)$ as a function of the line-of-sight positional uncertainty σ_r for $z = 1$ and 3 redshift bins. CMB and SDSS data are included in each redshift bin. Here 1% of $\sigma_z/(1 + z)$ corresponds to $34\,h^{-1}$ Mpc at $z = 1$ and $27\,h^{-1}$ Mpc at $z = 3$.

Table 11 shows the propagated errors on dark energy parameters for ΛCDM. The left-hand panel of Figure 9 shows the corresponding error ellipses. The errors on w_0 and w_1 using photometric redshifts increase by a factor of ~2.4 with the baseline survey parameters (V1N1) relative to spectroscopic results, while $w(z_{\rm pivot})$ is less affected. As shown in Figure 9, this is because the ellipse is more elongated with relatively little increase in its minor axis compared to the left-hand panel of Figure 5. This is due to the increased dominance of the $z \sim 1$ survey over $z = 3$. The value of $z_{\rm pivot}$ increases slightly with photometric redshift data. As shown in Figure 3, $D_A(z)$ at higher z contributes more to the information compared to $H(z)$. Thus,

TABLE 10
MARGINALIZED ERRORS ON $D_A(z)$ AND $H(z)$ FOR PHOTOMETRIC REDSHIFT SURVEYS

SURVEYS			REDSHIFT					
$z \sim 1$	$z = 3$	PARAMETER	0.3	0.6	0.8	1.0	1.2	3.0
V1N1	V1N1	$D_A(z)$	5.19	6.98	4.84	4.25	3.90	2.26
		$H(z)$	5.80	22.37	19.58	18.28	17.77	16.15
V1N5	V1N5	$D_A(z)$	5.19	4.84	3.26	2.81	2.56	1.57
		$H(z)$	5.80	16.33	14.29	13.27	12.88	10.11
V5N5	V5N5	$D_A(z)$	5.19	3.14	2.19	1.93	1.77	1.06
		$H(z)$	5.80	10.02	8.78	8.21	7.99	7.26

NOTES.—The fractional percentage error on the cosmological distances under conditions appropriate to photometric redshifts. The redshift accuracy has been degraded to 1% (1 σ) on $\sigma_z/(1 + z) = \Delta\lambda/\lambda$, i.e., $\sigma_z = 2\%$ at $z = 1$ and 4% at $z = 3$. The results will scale as $\sigma_z^{1/2}$, and σ_z would typically be larger for actual photometric redshifts. The left two columns show variations in the survey parameters. V1N1 is the baseline survey volume and number density. V1N5 allows for a fivefold increase in the number density. V5N5 is 5 times more volume at the baseline number density. CMB and SDSS are included in all sets. For SDSS, the baseline survey parameters (V1N1) are used and spectroscopic redshifts ($\sigma_z = 0$) are adopted. The ΛCDM fiducial model is used.

TABLE 11
MARGINALIZED ERRORS FOR ΛCDM FOR PHOTOMETRIC REDSHIFT SURVEYS

$z \sim 1$	$z = 3$	$\sigma_{\Omega_m h^2}/\Omega_m h^2$	σ_{Ω_x}	σ_{w_0}	σ_{w_1}	$z_{\rm pivot}$	$\sigma_{w_{z,\rm pivot}}$
V1N1		0.0091	0.0799	0.613	0.704	0.834	0.175
V1N5		0.0089	0.0736	0.534	0.578	0.887	0.150
	V1N1	0.0090	0.0859	0.752	0.979	0.735	0.218
	V1N5	0.0089	0.0820	0.670	0.855	0.742	0.217
V1N1	V1N1	0.0088	0.0777	0.584	0.668	0.834	0.175
V1N5	V1N5	0.0085	0.0708	0.504	0.544	0.887	0.148
V5N5	V5N5	0.0077	0.0592	0.413	0.437	0.904	0.118
V10N10	V10N10	0.0069	0.0485	0.335	0.352	0.912	0.094
V10N50	V10N50	0.0062	0.0375	0.256	0.267	0.921	0.071
V20N20	V20N20	0.0060	0.0379	0.261	0.276	0.908	0.073

NOTES.—Redshift uncertainties have been applied as in Table 10: 1% in $\sigma_z/(1+z)$. Various survey sizes are investigated, as detailed in the left two columns. V numbers specify the change in the survey volume, N the change in the number of galaxies. Note that V20 is 20,000 deg^2 at $z \sim 1$ and about 3000 deg^2 at $z \sim 3$. Blanks indicate that a survey has been excluded. Larger redshift uncertainties can be offset with more volume; for example, 4% errors in $\sigma_z/(1+z)$ would require 4 times more volume to produce the results in this table. CMB and SDSS are included in all rows. For SDSS, the baseline survey parameters (V1N1) with spectroscopic redshifts are used in all cases.

eliminating $H(z)$ by using photometric redshifts will weight higher redshifts slightly more.

Table 11 also shows that increasing $V_{\rm survey}$ 20-fold (V20N20) or 10-fold with a fivefold increase in target density n (V10N50) allows the results from photometric redshift surveys to achieve the accuracy of the spectroscopic redshift surveys. This corresponds to 10,000 or 20,000 deg^2 of sky at $z = 1$ (with 1% errors in $1 + z$). Observationally, increasing the number density by 5 times (V10N50) will be more difficult than doubling the survey area because the galaxy luminosity function flattens out around this number density, so that $\sqrt{2}$ in depth is far less than a factor of 5 in source counts. The errors of w_0 and w_1 do not scale trivially with $V_{\rm survey}^{1/2}$ because the SDSS and CMB survey parameters are being held fixed.

Results including the SN survey data are shown in Table 12. With SNe, improving the redshift survey condition to between V5N5 and V10N10 allows the photometric redshift survey to recover the spectroscopic result in Table 5. This is equivalent to an imaging survey of about 30,000 deg^2 with 4% photometric redshift error at $z \sim 1$ and a depth to reach 1000 $z \sim 1$ galaxies per square degree. Surveys such as Pan-STARRS[1] or the Large Synoptic Survey Telescope[2] could achieve this.

Tables 13 and 14 show the same analysis as Tables 11 and 12, but for model 2 ($w = -\frac{2}{3}$) instead of ΛCDM. The

[1] See http://pan-starrs.ifa.hawaii.edu.
[2] See http://www.lsst.org.

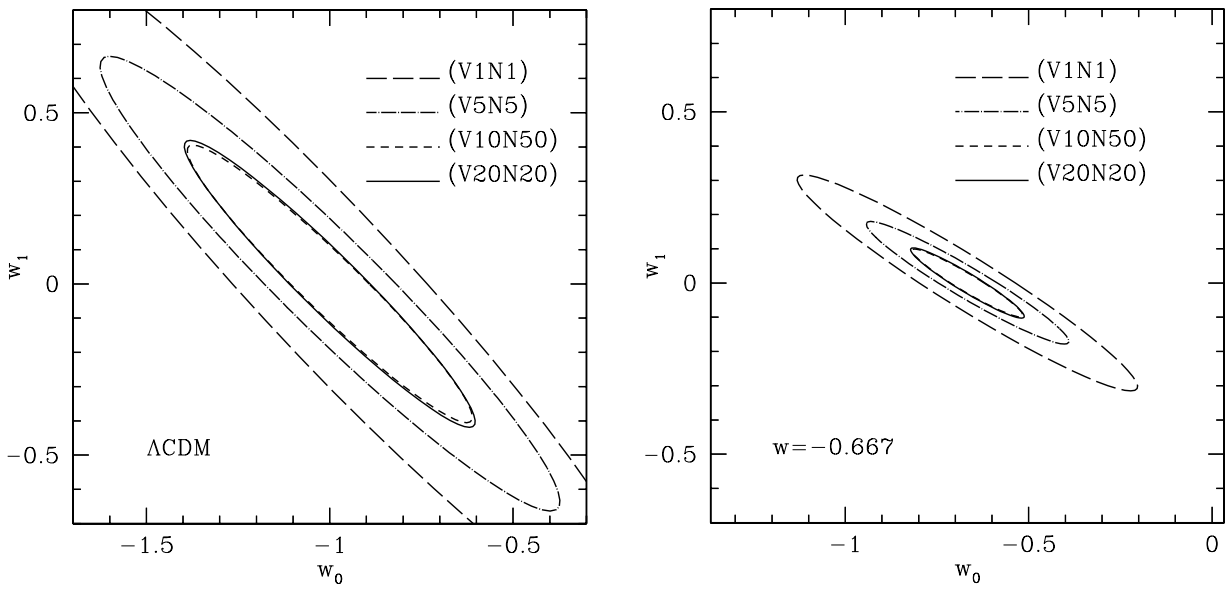

FIG. 9.—Elliptical error regions for w_0 and w_1 for photometric redshift surveys with 1% of $\sigma_z/(1+z)$ ($\sigma_z = 0.02$ for $z \sim 1$, $\sigma_z = 0.04$ for $z = 3.0$). *Left*: ΛCDM. *Right*: Model 2 ($w = -\frac{2}{3}$). CMB data and all redshift surveys are included in all cases. The survey parameters written inside the parentheses are for both $z \sim 1$ and $z = 3$ bins. V numbers specify the change in the survey volume relative to the baseline, N the change in the number of galaxies. For SDSS, the baseline survey parameters (V1N1) with spectroscopic redshifts are used. In both figures, V10N50 is nearly the same as V20N20.

TABLE 12
MARGINALIZED ERRORS FOR ΛCDM FOR PHOTOMETRIC REDSHIFT SURVEY WITH SNe

$z \sim 1$	$z = 3$	$\sigma_{\Omega_m h^2}/\Omega_m h^2$	σ_{Ω_x}	σ_{w_0}	σ_{w_1}	$z_{\rm pivot}$	$\sigma_{w_{z,\rm pivot}}$
		0.0093	0.0088	0.116	0.231	0.478	0.035
V1N1		0.0089	0.0085	0.106	0.212	0.473	0.034
V1N5		0.0087	0.0083	0.098	0.195	0.470	0.034
	V1N1	0.0090	0.0087	0.114	0.229	0.477	0.034
	V1N5	0.0087	0.0086	0.113	0.227	0.476	0.034
V1N1	V1N1	0.0086	0.0084	0.105	0.211	0.473	0.034
V1N5	V1N5	0.0083	0.0082	0.097	0.193	0.470	0.033
V5N5	V5N5	0.0073	0.0080	0.087	0.171	0.471	0.032
V10N10	V10N10	0.0065	0.0078	0.077	0.148	0.478	0.031
V10N50	V10N50	0.0060	0.0076	0.066	0.119	0.496	0.030
V20N20	V20N20	0.0058	0.0076	0.068	0.124	0.495	0.030

NOTE.—As Table 11, but the SN data have also been included.

TABLE 13
MARGINALIZED ERRORS FOR MODEL 2 FOR PHOTOMETRIC REDSHIFT SURVEYS

$z \sim 1$	$z = 3$	$\sigma_{\Omega_m h^2}/\Omega_m h^2$	σ_{Ω_x}	σ_{w_0}	σ_{w_1}	$z_{\rm pivot}$	$\sigma_{w_{z,\rm pivot}}$
V1N1		0.0091	0.0637	0.395	0.278	1.383	0.087
V1N5		0.0090	0.0563	0.332	0.224	1.452	0.069
	V1N1	0.0092	0.0618	0.342	0.249	1.285	0.122
	V1N5	0.0090	0.0590	0.284	0.187	1.376	0.119
V1N1	V1N1	0.0090	0.0545	0.305	0.207	1.412	0.086
V1N5	V1N5	0.0087	0.0457	0.245	0.160	1.476	0.068
V5N5	V5N5	0.0079	0.0346	0.182	0.118	1.476	0.053
V10N10	V10N10	0.0071	0.0264	0.138	0.090	1.463	0.041
V10N50	V10N50	0.0064	0.0191	0.099	0.065	1.453	0.030
V20N20	V20N20	0.0063	0.0195	0.102	0.067	1.436	0.032

NOTE.—As Table 11, but fiducial model 2 ($w = -2/3$) has been used.

TABLE 14
MARGINALIZED ERRORS FOR MODEL 2 FOR PHOTOMETRIC REDSHIFT SURVEYS WITH SNe

$z \sim 1$	$z = 3$	$\sigma_{\Omega_m h^2}/\Omega_m h^2$	σ_{Ω_x}	σ_{w_0}	σ_{w_1}	$z_{\rm pivot}$	$\sigma_{w_{z,\rm pivot}}$
		0.0094	0.0134	0.087	0.122	0.682	0.023
V1N1		0.0091	0.0104	0.066	0.089	0.695	0.023
V1N5		0.0089	0.0091	0.057	0.072	0.716	0.023
	V1N1	0.0091	0.0120	0.076	0.107	0.678	0.023
	V1N5	0.0089	0.0112	0.068	0.095	0.676	0.023
V1N1	V1N1	0.0088	0.0100	0.062	0.084	0.693	0.023
V1N5	V1N5	0.0086	0.0088	0.053	0.067	0.713	0.023
V5N5	V5N5	0.0077	0.0079	0.046	0.054	0.743	0.022
V10N10	V10N10	0.0070	0.0073	0.041	0.044	0.799	0.021
V10N50	V10N50	0.0063	0.0068	0.037	0.035	0.904	0.019
V20N20	V20N20	0.0062	0.0069	0.038	0.037	0.881	0.020

NOTE.—As Table 11, but fiducial model 2 ($w = -2/3$) has been used and SN data are included.

degradation of performance relative to the spectroscopic case is similar. Like the ΛCDM case, V10N50 or V20N20 recovers the spectroscopic result without SNe, and V5N5 or V10N10 does the job with SNe. The right-hand panel of Figure 9 shows the corresponding error ellipses.

Therefore, after considering both the projection and power suppression effects of redshift uncertainties, we expect that, when combined with SN data, surveys with 4% errors on $1 + z$ and roughly 30 times more volume than our baseline surveys will be equivalent to the spectroscopic surveys. As this is essentially the full sky at $z \sim 1$, improving beyond these levels will require better redshift accuracy.

5. CONCLUSION

Understanding the acceleration of the universe is one of the most important problems in both cosmology and fundamental particle physics. Identifying the physical cause,

whether dark energy or some alteration to the theory of gravitation, is certain to be a major breakthrough. Precision measurements of the expansion history of the universe could be crucial in choosing between alternative theories. In this paper we demonstrated that a standard ruler test using baryonic acoustic oscillations imprinted in the large-scale structure could be a superb probe of the acceleration history. The oscillations in the galaxy power spectrum are expected to be robust against contamination from clustering bias, redshift distortions, and other broadband systematic errors.

We have studied the performance that could be achieved on dark energy models from the measurement of the acoustic oscillations in large galaxy spectroscopic surveys at redshifts 0.3, 1, and 3. The $z \sim 1$ baseline survey uses 900,000 galaxies to probe 1.7 h^{-3} Gpc^3; the $z = 3$ survey uses a half-million galaxies to cover 0.5 h^{-3} Gpc^3. While these numbers are large, the number densities are not, which means that relatively bright galaxies could be used. Using a Fisher matrix treatment of the statistical errors that result from the three-dimensional power spectra, as well as CMB and SNe data, we forecasted errors on the distances along and across the line of sight and then projected these measurements of $H(z)$ and $D_A(z)$ onto dark energy parameters. Of course, the cosmographical performances are independent of the details of the dark energy model. We summarize our major results below.

First, we have shown that (1 σ) errors of 0.037 on Ω_X, 0.10 on $w(z = 0.8)$, and 0.28 on dw/dz are achievable for ΛCDM when CMB provides the scale of the baryonic oscillations. The constraints on dw/dz are comparable to those from the luminosity distances of future SN data. Most constraints were contributed by information in the higher redshift surveys ($z \gtrsim 0.6$) because the baryonic oscillations in the power spectrum are better preserved against nonlinearity at higher redshift. When we combined the redshift survey data with the SN data, the constraints were improved to 0.16 on dw/dz.

Second, we found that fiducial dark energy models with less negative w than ΛCDM improve overall performance and also favor the galaxy redshift surveys relative to the SN data. Together, a 0.05 measurement of dw/dz is achieved!

Third, we discussed how the quality of constraints depends on the survey volume and number density. Increasing the survey volume with the number density fixed always gives the better result by $V_{\rm survey}^{1/2}$. Increasing the number density, that is, going deeper with the volume fixed, will also improve the constraints but with asymptotic saturation. Changing the survey volume with a fixed total number of objects has a maximum in performance that is close to the baseline values.

Fourth, we computed how well an imaging survey with photometric redshifts could measure the acoustic oscillations. We find that errors of 0.25% in $1 + z$ are necessary to retain information on the Hubble parameter $H(z)$. However, redshift errors of 4% in $1 + z$ can be tolerated without losing the oscillations to projection effects, and the angular diameter distance could be measured as a function of redshift. We estimate that a survey 20 times larger than our baseline but with 1% redshift error on $1 + z$ is needed to replace the spectroscopy but that the requirement drops to 5–10 times larger when combined with the constraints from SNe. The 4% redshift errors require 4 times more volume.

To date, much of the attention in cosmological probes of acceleration has rightly been given to the studies of distant SNe. The acoustic oscillations in the galaxy power spectrum have not even been conclusively detected yet. Nevertheless, we are encouraged by the result that the study of acoustic oscillations in large galaxy surveys can achieve comparable performance to upcoming SN data sets. Given the mystery and importance of the acceleration of the universe, it is crucial to have multiple experiments with independent systematic errors. Moreover, the ability to measure $H(z)$ directly and to probe the expansion at higher redshifts ($z \approx 3$) opens the possibility of detecting new surprises. Although the cosmological constant model is most easily probed at lower redshifts, given the woeful history of theoretical predictions for dark energy, it seems to us unwise to design experiments based too closely on the assumptions of ΛCDM.

While the required redshift surveys are large, they are feasible within the current decade. Ground-based 8 m telescopes are sufficiently sensitive but currently lack the necessary highly multiplexed wide-field spectroscopic capability. Instruments such as the KAOS concept[3] could perform these surveys in about a year of observing. The surveys would of course have many other science applications, both for the study of galaxy evolution and for the search for more speculative features of the linear perturbations, e.g., primordial non-Gaussianity or additional preferred scales. At $z = 3$, the reach into the linear regime on intermediate scales exceeds even that of the CMB. Hence, we conclude that such surveys are attractive options for the study of large-scale structure over the next decade.

We thank Chris Blake, Arjun Dey, Karl Glazebrook, Eric Linder, and Saul Perlmutter for useful discussions. H.-J. S. was supported by a University of Arizona College of Science Graduate Fellowship. D. J. E. is supported by National Science Foundation grant AST 00-98577 and by an Alfred P. Sloan Research Fellowship.

[3] See http://www.noao.edu/kaos.

REFERENCES

Adelberger, K. L., Steidel, C. C., Giavalisco, M., Dickinson, M., Pettini, M., & Kellogg, M. 1998, ApJ, 505, 18
Alcock, C., & Paczynski, B. 1979, Nature, 281, 358
Aldering, G., et al. 2002, Proc. SPIE, 4835, 146
Armendariz-Picon, C., Mukhanov, V., & Steinhardt, P. J. 2000, Phys. Rev. Lett., 85, 4438
Ballinger, W. E., Peacock, J. A., & Heavens, A. F. 1996, MNRAS, 282, 877
Baugh, C. M., & Efstathiou, G. 1994, MNRAS, 267, 323
Bennett, C., et al. 2003, ApJS, 148, 1
Benoît, A., et al. 2003, A&A, 399, L19
Bilic, N., Tupper, G. B., & Viollier, R. D. 2002, Phys. Lett. B, 535, 17
Blake, C., & Glazebrook, K. 2003, ApJ, 594, 665
Bond, J. R., & Efstathiou, G. 1984, ApJ, 285, L45
Bond, J. R., Efstathiou, G., & Tegmark, M. 1997, MNRAS, 291, L33
Bond, J. R., & Szalay, A. 1983, ApJ, 274, 443
Boyle, L. A., Caldwell, R. R., & Kamionkowski, M. 2002, Phys. Lett. B, 545, 17
Bucher, M., & Spergel, D. N. 1999, Phys. Rev. D, 60, 043505
Caldwell, R. R., Dave, R., & Steinhardt, P. J. 1998, Ap&SS, 261, 303
Carroll, S. M., Press, W. H., & Turner, E. L. 1992, ARA&A, 30, 499
Coles, P. 1993, MNRAS, 262, 1065
Coles, P., Melott, A. L., & Munshi, D. 1999, ApJ, 521, L5
Cooray, A., Hu, W., Huterer, D., & Joffre, M. 2001, ApJ, 557, L7
Cooray, A., & Huterer, D. 1999, ApJ, 513, L95
de Bernardis, P., et al. 2000, Nature, 404, 955
Deffayet, C., Dvali, G., & Gabadadze, G. 2002, Phys. Rev. D, 65, 044023
Dekel, A., & Lahav, O. 1999, ApJ, 520, 24
Efstathiou, G., et al. 2002, MNRAS, 330, L29

Eisenstein, D. J. 2003, in ASP Conf. Ser. 280, Wide-Field Multi-Object Spectroscopy, ed. A. Dey (San Francisco: ASP), 35
Eisenstein, D. J., & Hu, W. 1998, ApJ, 496, 605
Eisenstein, D. J., Hu, W., & Tegmark, M. 1998, ApJ, 504, L57
———. 1999, ApJ, 518, 2
Eisenstein, D. J., et al. 2001, AJ, 122, 2267
Feldman, H. A., Kaiser, N., & Peacock, J. A. 1994, ApJ, 426, 23
Freese, K., & Lewis, M. 2002, Phys. Lett. B, 540, 1
Frieman, J. A., Hill, C. T., Stebbins, A., & Waga, I. 1995, Phys. Rev. Lett., 75, 2077
Frieman, J. A., Huterer, D., Linder, E. V., & Turner, M. S. 2003, Phys. Rev. D, 67, 083505
Gawiser, E., & Silk, J. 1998, Science, 280, 1405
Gu, J., & Hwang, W. 2001, Phys. Lett. B, 517, 1
Haiman, Z., Mohr, J. J., & Holder, G. P. 2001, ApJ, 553, 545
Halverson, N. W., et al. 2002, ApJ, 568, 38
Hamilton, A. J. S. 1998, in The Evolving Universe, ed. D. Hamilton (Dordrecht: Kluwer), 185
Hanany, S., et al. 2000, ApJ, 545, L5
Hatton, S., & Cole, S. 1999, MNRAS, 310, 1137
Heavens, A. F., & Taylor, A. N. 1997, MNRAS, 290, 456
Holtzman, J. A. 1989, ApJS, 71, 1
Hu, W., Eisenstein, D. J., & Tegmark, M. 1998, Phys. Rev. Lett., 80, 5255
Hu, W., & Haiman, Z. 2003, Phys. Rev. D, 68, 063004
Hu, W., & Sugiyama, N. 1996, ApJ, 471, 542
Hui, L., Stebbins, A., & Burles, S. 1999, ApJ, 511, L5
Huterer, D., & Starkman, G. 2003, Phys. Rev. Lett., 90, 031301
Huterer, D., & Turner, M. S. 1999, Phys. Rev. D, 60, 1301
———. 2001, Phys. Rev. D, 64, 123527
Jain, B., & Bertschinger, E. 1994, ApJ, 431, 495
Jungman, G., Kamionkowski, M., Kosowsky, A., & Spergel, D. N. 1996, Phys. Rev. D, 54, 1332
Kaiser, N. 1986, MNRAS, 219, 785
———. 1987, MNRAS, 227, 1
Kasuya, S. 2001, Phys. Lett. B, 515, 121
Knox, L. 1995, Phys. Rev. D, 52, 4307
Kujat, J., Linn, A. M., Scherrer, R. J., & Weinberg, D. H. 2002, ApJ, 572, 1
Lange, A. E., et al. 2001, Phys. Rev. D, 63, 2001
Limber, D. N. 1953, ApJ, 117, 134
Linder, E. V. 2003a, Phys. Rev. D, submitted
———. 2003b, Phys. Rev. Lett., 90, 1301
Linder, E. V., & Huterer, D. 2003, Phys. Rev. D, 67, 081303
Maor, I., Brustein, R., McMahon, J., & Steinhardt, P. J. 2002, Phys. Rev. D, 65, 123003
Maor, I., Brustein, R., & Steinhardt, P. J. 2001, Phys. Rev. Lett., 86, 6
Matsubara, T., & Szalay, A. S. 2002, ApJ, 574, 1
———. 2003, Phys. Rev. Lett., 90, 21302
Meiksin, A., & White, M. 1999, MNRAS, 308, 1179
Meiksin, A., White, M., & Peacock, J. A. 1999, MNRAS, 304, 851
Miller, A. D., et al. 1999, ApJ, 524, L1
Miller, C., Nichol, R. C., & Batuski, D. J. 2001, ApJ, 555, 68
Newman, J. A., & Davis, M. 2000, ApJ, 534, L11
Newman, J. A., Marinoni, C., Coil, A. L., & Davis, M. 2002, PASP, 114, 29
Peebles, P. J. E., & Yu, J. T. 1970, ApJ, 162, 815
Percival, W., et al. 2001, MNRAS, 327, 1297
Perlmutter, S., et al. 1999, ApJ, 517, 565
Popa, L. A., Burigana, C., & Mandolesi, N. 2001, ApJ, 558, 10
Ratra, B., & Peebles, P. J. E. 1988, Phys. Rev. D, 37, 3406
Riess, A. G., et al. 1998, AJ, 116, 1009
———. 2001, ApJ, 560, 49
Scherrer, R. J., & Weinberg, D. H. 1998, ApJ, 504, 607
Scott, D., Silk, J., & White, M. 1995, Science, 268, 829
Seljak, U. 2000, MNRAS, 318, 203
Spergel, D. N. S., et al. 2003, ApJS, 148, 175
Steidel, C. C., Adelberger, K. L., Dickinson, M., Giavalisco, M., Pettini, M., & Kellogg, M. 1998, ApJ, 492, 428
Steidel, C. C., Giavalisco, M., Pettini, M., Dickinson, M., & Adelberger, K. L. 1996, ApJ, 462, L17
Steinhardt, P. J. 1997, in Critical Dialogues in Cosmology, ed. N. Turok (Singapore: World Scientific), 407
Taylor, A. N., & Watts, P. I. R. 2001, MNRAS, 328, 1027
Tegmark, M. 1997, Phys. Rev. Lett., 79, 3806
———. 2001, Phys. Rev. D, 66, 103507
Tegmark, M., Taylor, A. N., & Heavens, A. F. 1997, ApJ, 480, 22
Tegmark, M., Zaldarriaga, M., & Hamilton, A. J. 2001, Phys. Rev. D, 63, 3007
Tonry, J. L., et al. 2003, ApJ, 594, 1
Turner, M. S., & White, M. 1997, Phys. Rev. D, 56, 443
Wang, Y., & Garnavich, P. M. 2001, ApJ, 552, 445
Wang, Y., Spergel, D. N., & Strauss, M. A. 1999, in AIP Conf. Proc. 478, Particle Physics and the Early Universe (COSMO-98), ed. D. O. Caldwell (New York: AIP), 164
Weller, J., & Albrecht, A. 2002, Phys. Rev. D, 65, 103512
York, D. G., et al. 2000, AJ, 120, 1579
Zaldarriaga, M., Spergel, D. N., & Seljak, U. 1997, ApJ, 488, 1
Zlatev, I., Wang, L., & Steinhardt, P. J. 1999, Phys. Rev. Lett., 82, 896